Solid State Laboratory
Research Triangle Institute
Post Office Box 490
Durham, North Carolina 27702

DIFFUSION PROCESS MODELING

Contract No. NAS8-20058

August 1965

Robert P. Donovan

Technical Summary Report

February 1965 to August 1965

Prepared for

George C. Marshall Space Flight Center
Astrionics Laboratory
National Aeronautics and Space Administration
Huntsville, Alabama 35812

FACILITY FORM 602

N66-17474	
(ACCESSION NUMBER)	(THRU)
79	1
(PAGES)	(CODE)
CR 70455	26
(NASA CR OR TMX OR AD NUMBER)	(CATEGORY)

GPO PRICE $ ________

CFSTI PRICE(S) $ ________

Hard copy (HC) 3.00

Microfiche (MF) .75

ff 653 July 65

RTI RESEARCH TRIANGLE INSTITUTE · DURHAM, NORTH CAROLINA

Foreword

This summary report was prepared by the Solid State Laboratory of the Research Triangle Institute under Contract No. NAS8-20058, "Improving Silicon Integrated Device Reliability by Modeling the Processes of Fabrication. I. Diffusion" and is a sequel to the final report of Contract No. NAS8-11243. Copies of this earlier report are available through Scientific and Technical Aerospace Reports (STAR). The present work began in February 1965, ended in August 1965, and was administered under the technical direction of the Astrionics Laboratory of the George C. Marshall Space Flight Center. Dr. A. M. Holladay was technical supervisor for the Astrionics Laboratory.

Abstract

17474

A model due to Smits, based on the existence of a rate limitation at the surface, has been used to relate the independent variables of diffusion (time, temperature, and impurity gas concentration) to the intermediate diffusion parameters (junction depth and sheet resistivity). Estimates of the surface rate parameter K in the Smits model are 0.3×10^{-2} μ/min at 1100°C and 0.6×10^{-2} μ/min at 1150°C for silicon employing a phosphine source diffusion system.

The flat band voltage of an oxidized silicon surface is shown to be a significant variable in determining the magnitude of junction reverse current. This variable can be monitored during device fabrication by contacting the oxidized surface with a silver probe whose tip has been dipped in mercury.

Table of Contents

List of Illustrations

List of Illustrations (Continued)

List of Tables

1. Introduction

Among the most important factors determining the performance of an electronic system are the fabrication processes used in its construction. The relationship between system performance and key process parameters is direct as indicated in Figure 1. To obtain better knowledge of the interdependence among the variables listed in the blocks of Figure 1, a program of developing semi-empirical models has been initiated. In this program the relationships between the blocks are empirically established, using a simple theory as the starting point. These semi-empirical relationships are the models which make possible the calculation of system performance in terms of the properties of the starting material and the processing parameters. Between blocks 1, 2 and 3 variables of processing such as listed in Fig. 1 are probably predominant, although this list is not yet complete. Beyond block 3 other factors clearly must be included such as circuit design and environment. These latter blocks are not the subject of this investigation.

Work initiated by MSFC under Contract No. NAS8-11243 (Ref. 1) investigated the relationships between block 1 and block 2 for the diffusion process, and, as a second step, the relationship between block 2 and block 3 for a planar diffused diode. This work, as reported in Ref. 1, resulted in simple mathematical models between blocks 1 and 2 in which the junction depth x_j and the sheet resistivity ρ_s of a diffused layer are expressed in terms of the time t, temperature T and impurity concentration c during a phosphine source diffusion. The models developed were subject to the following limitations:

1. The only substrate resistivity investigated has been 1 ohm-cm p-type silicon;
2. The oxygen concentration during diffusion has been maintained at a constant 6700 ppm;
3. The range of the three process variables investigated has been restricted to:

$$1100°\mathrm{C} \leq T \leq 1200°\mathrm{C}$$

$$15 \text{ min} \leq t \leq 60 \text{ min}$$

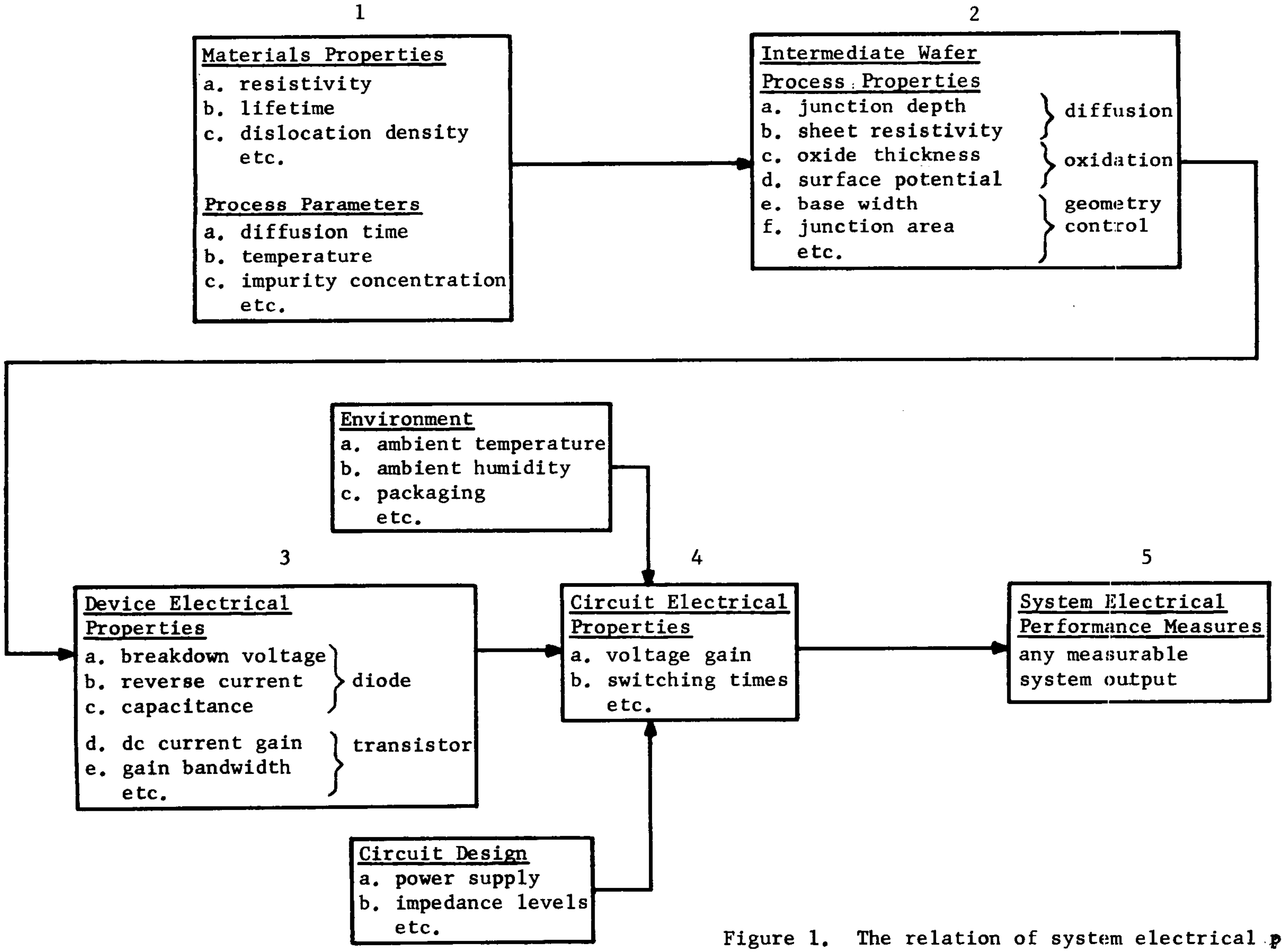

Figure 1. The relation of system electrical performance to the starting material properties and the variables of fabrication.

$$35 \text{ ppm} \leq c \leq 2450 \text{ ppm}$$

The work described in this final report is an extension of this investigation. The purpose of this extension was to implement the steps described in the conclusions and recommendations of the final report of the original contract (Ref. 1, pp. 54-55):

"Specific next steps in the program are the concurrent investigations of:

1. Methods of improving control over diffusions at impurity concentrations of 35 ppm and less. A direct measurement of P_2O_5 concentration in the neighborhood of the silicon being diffused is quite desirable.
2. Significant surface related measurements to incorporate into the models for breakdown voltage and reverse current of a planar, diffused diode. Control of any measurement so identified in terms of processing variables is an important but subsequent problem.
3. Models which are likely to be suitable over a wider range to be more exact than the present ones."

Each of these recommended investigations is discussed in this report: No. 3 in Secs. 2 and 4; No. 1 in Sec. 3; and No. 2 in Sec. 5. Conclusions from the present work and recommendations for the future course of the program are given in Sec. 6.

2. Model Improvement

The Smits solution (Ref. 2) to the one dimensional diffusion equation, assuming a finite rate limitation at the surface, was given in Ref. 1 as:

$$N(y,z) = N_{eq}\left(\mathrm{erfc}(y) - e^{(y+z)^2-y^2}\, \mathrm{erfc}(y+z)\right) \tag{1}$$

where

$$y = \frac{x}{2\sqrt{Dt}} ,$$

$$z = \frac{K}{D}\sqrt{Dt} = K\sqrt{\frac{t}{D}} .$$

For the discussion to follow this notation has been altered as follows:

$u \equiv \dfrac{x}{x_j}$, $\quad x_j$ = depth at which the concentration of the diffusing impurities is equal to the impurity concentration of the starting silicon.

$A \equiv \dfrac{x_j}{2\sqrt{Dt}}$,

$B \equiv \dfrac{K}{D}\sqrt{Dt} = K\sqrt{\dfrac{t}{D}}$,

$\mathrm{erq}\ v \equiv e^{v^2}\ \mathrm{erfc}\ v$ (erq is a new function hereby defined for convenience (Ref. 3)).

Equation 1 then becomes

$$N = N_{eq}\{e^{-(uA)^2}\ \mathrm{erq}\ uA - \mathrm{erq}(uA + B)\} \equiv N_{eq}\ F(uA,B) . \tag{2}$$

The surface is at u = 0, so that the surface concentration is

$$N_o = N_{eq}\ F(0,B) = N_{eq}\{1 - \mathrm{erq}\ B\} . \tag{3}$$

For B >> 1(erq B→0 and $K >> \sqrt{\frac{D}{t}}$), $N_o \simeq N_{eq}$ and $N \simeq N_{eq}$ erfc uA which is the usual erfc equation.

The average impurity concentration is

$$\bar{N} \equiv \frac{1}{x_j}\int_o^{x_j} N dx = N_{eq}\int_o^1 F(uA,B)du \equiv N_{eq}\, E(A,B) \ . \qquad (4)$$

At the junction (u = 1) N = N_B (the substrate impurity concentration) and from Eq. 2

$$\frac{N_B}{N_{eq}} = F(A,B) \qquad (5)$$

The net impurity concentration (n) is the difference between the diffusing impurity concentration and the background impurity concentration. In terms of the Smits model (Eqs. 1 - 5) the net impurity concentration is given by:

$$n = N - N_B = N_{eq}\big(F(uA,B) - F(A,B)\big) \ . \qquad (6)$$

Similarly the average net impurity concentration ($\bar{n}$) is the difference between the average diffusing impurity concentration and the background concentration:

$$\bar{n} = \bar{N} - N_B = N_{eq}\big(E(A,B) - F(A,B)\big) \qquad (7)$$

To account for the reported differences between total impurity concentration and the electrically active impurity concentration (Refs. 4,5), the impurity distribution predicted by Eq. 2 was altered to that of a truncated Smits distribution as sketched in Fig. 2.

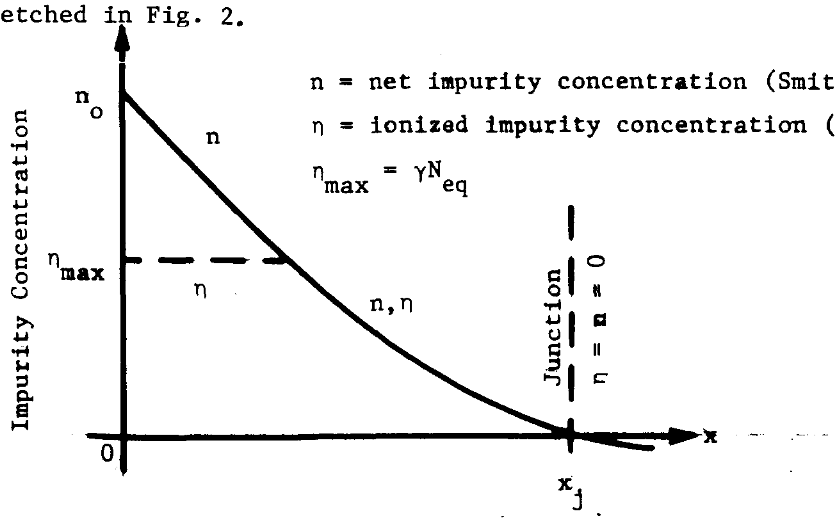

Fig. 2. The truncated Smits distribution

The ionized impurity concentration η is now given by:

$$\eta = N_{eq}\,\tilde{F}(uA,B);\ \tilde{F}(uA,B) = F(uA,B) - F(A,B) \text{ or } \gamma, \text{ whichever is less}. \qquad (8)$$

In Eqs. 6 and 7, η is now used instead of N. For $\tilde{F}(uA,B)$ less than γ, these functions are the same as before; when $\tilde{F}(uA,B)$ is greater than γ, the impurity distribution is assumed to correspond to the flattened-out region of Fig. 2. γ is less than or equal to one and $N_{eq}\,\gamma$ is the maximum concentration of phosphorus that can be detected by the four point probe. It is of consequence only at high doping levels (Refs. 4,5)--doping levels at which the actual phosphorus concentration exceeds the maximum that can be detected electrically ($\sim 6 \times 10^{20}$ cm^{-3}).

Using two computer approximations for the erfc function, values of E, F, $J(\equiv \frac{\bar{\eta}}{N_B})$ and other functions were tabulated over the following ranges of A, B, and γ:

$A = 0.0(0.2)\ 3.8$

$B = 1,2,5$ decades from 10^{-2} to 10

$u = 0.0(0.2)\ 1.2, \infty$

$\gamma = 0.05, 0.1, 0.2, 0.5, 1$

From this huge quantity of computed numbers, various plots have been prepared to illustrate the general features of the truncated Smits distribution. Figure 3 is a plot of $\frac{N_B}{\bar{\eta}}$ vs A for various values of B and γ. As B increases, the Smits distribution approaches that of the erfc. The erfc distribution is in fact a special case of the Smits model. These same curves are plotted in Fig. 4 on erfc paper.

The effect of truncating the Smits model is most pronounced at large values of B as shown in Fig. 5.

Plots of various functions that can be compared with measured data of diffused layers appear in Figs. 6 and 7. In these plots

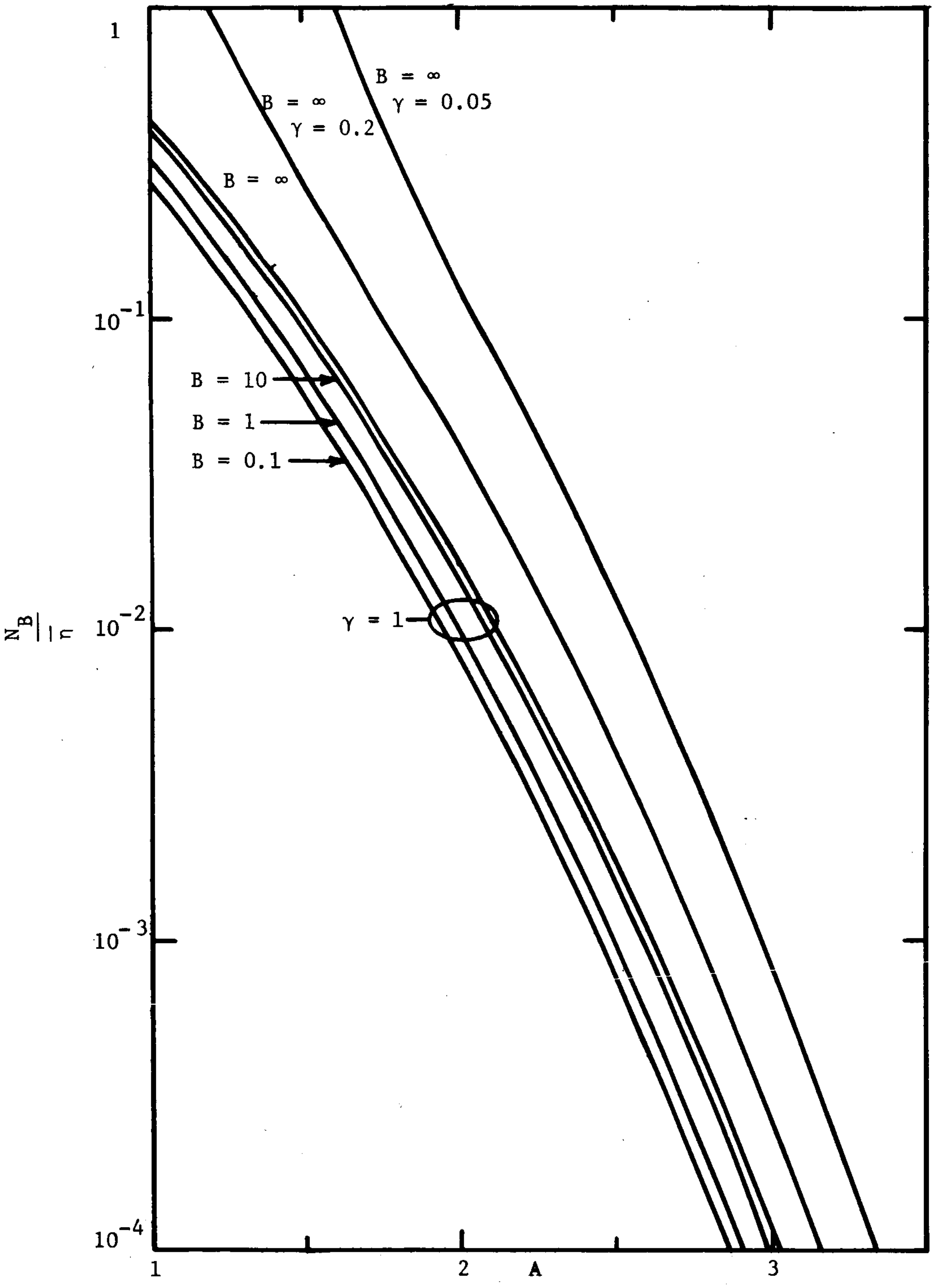

Fig. 3. Plot of $\frac{N_B}{\bar{\eta}}$ as a function of A for various values of B and γ

$\xi \equiv x_j \frac{K}{D}$ is a generalized junction depth

$\tau \equiv t \frac{K^2}{D}$ is a generalized time.

A closed form expression for η is given in Appendix A.

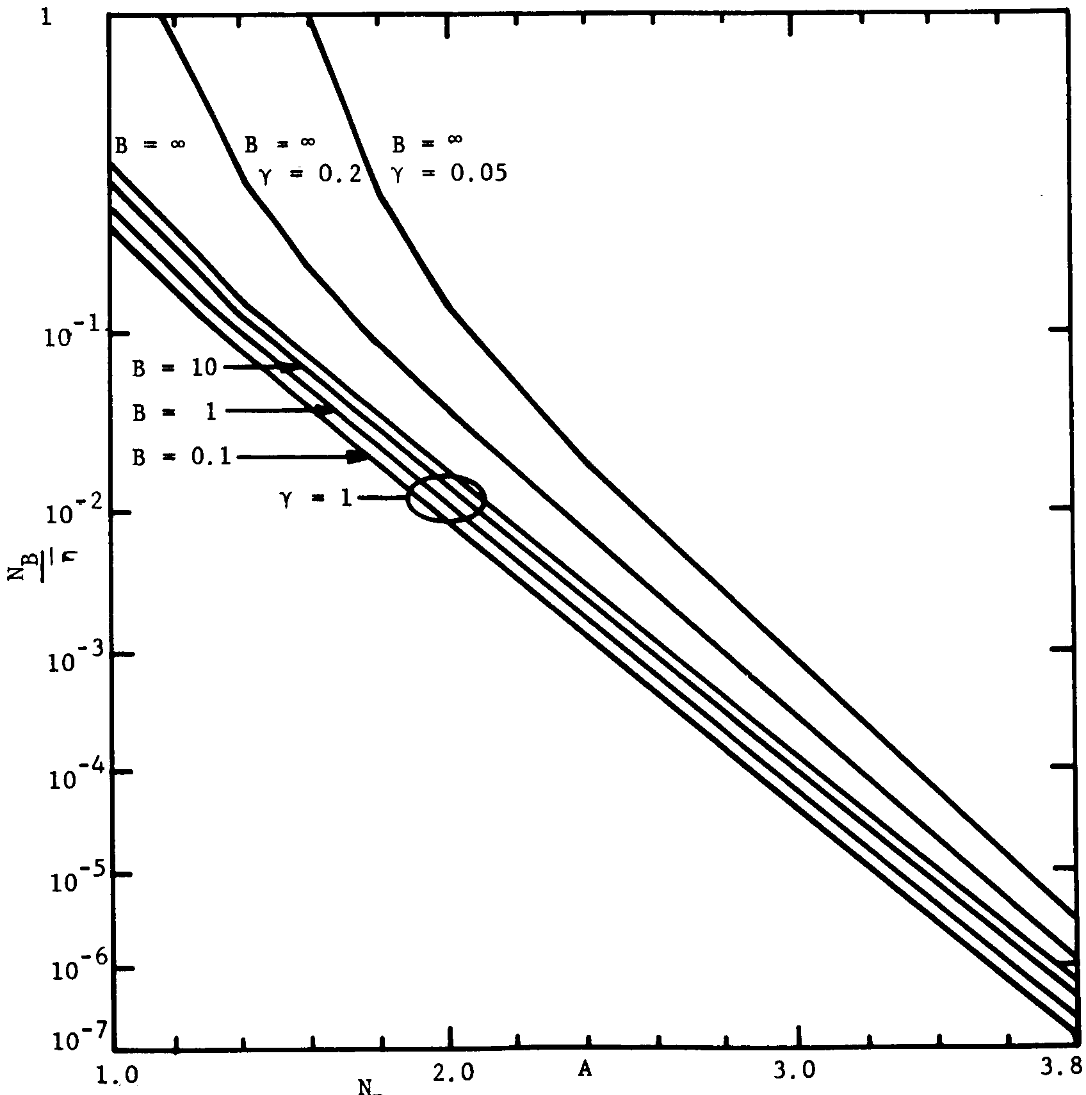

Fig. 4. Plot of $\frac{N_B}{\bar{\eta}}$ vs A, using an erfc scale for the ordinate

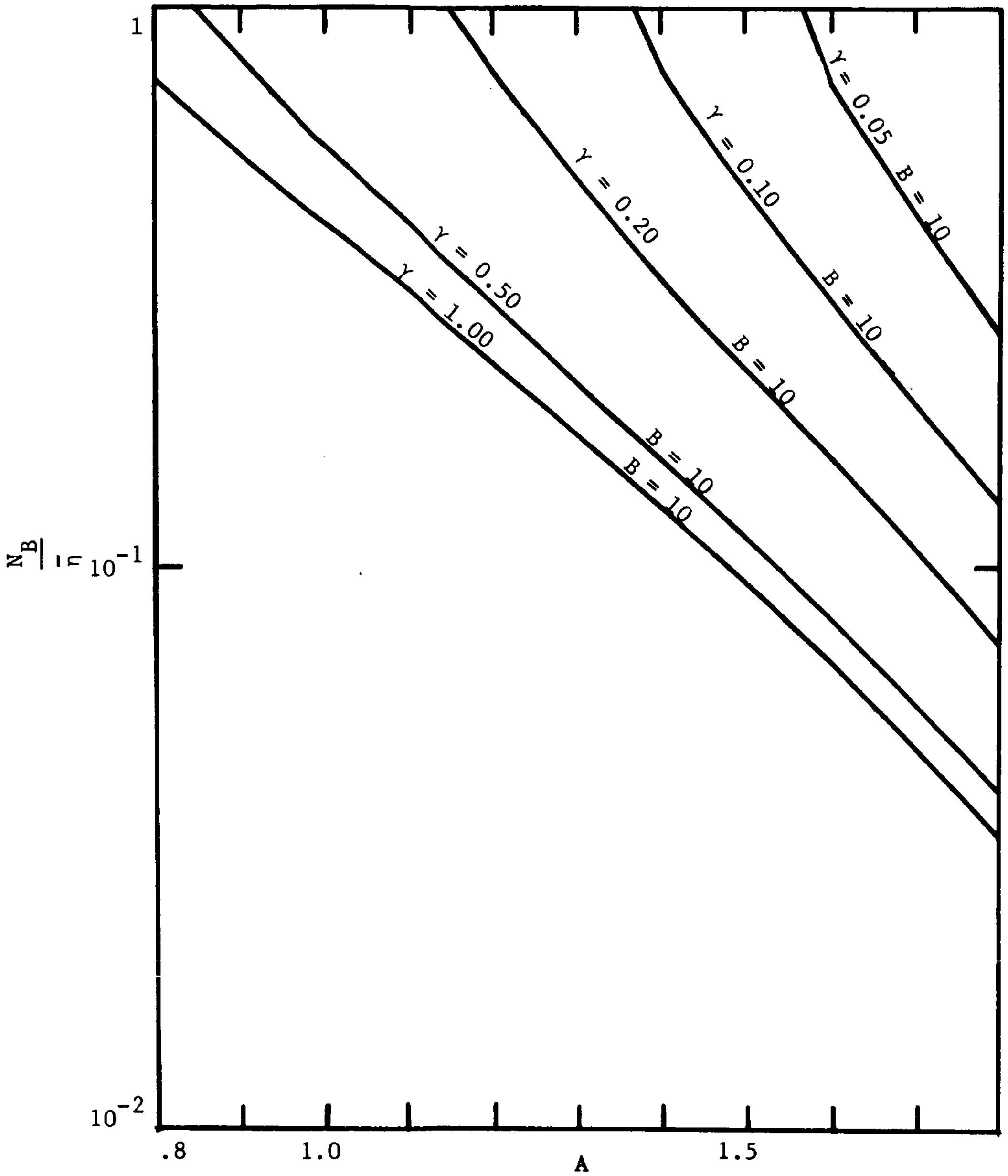

Fig. 5a. The influence of γ upon $\frac{N_B}{\bar{\eta}}$ for B = 10

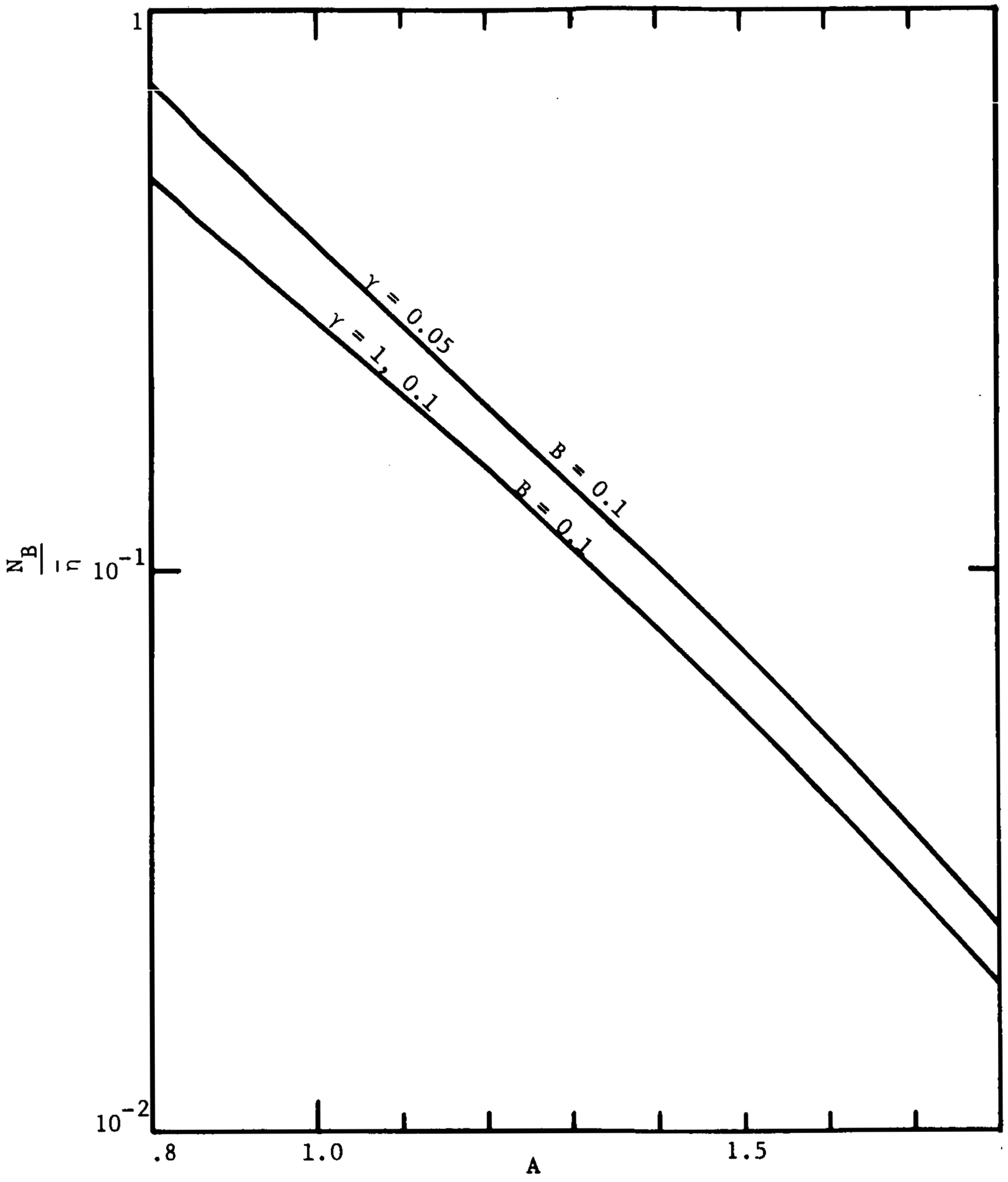

Fig. 5b. The influence of γ upon $\frac{N_B}{\bar{\eta}}$ for B = 0.1

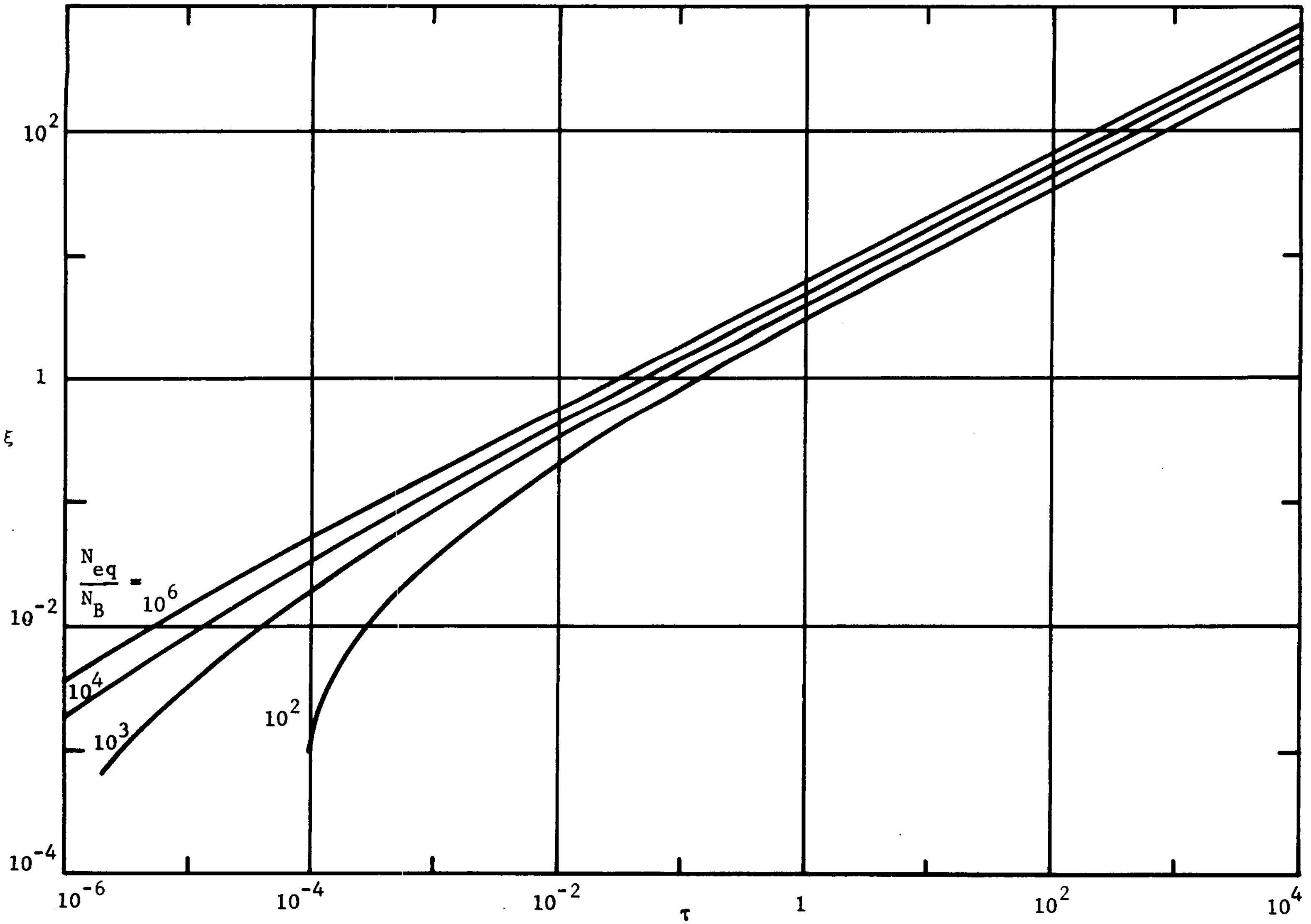

Fig. 6. Generalized junction depth vs generalized time of diffusion predicted by the Truncated Smits Model

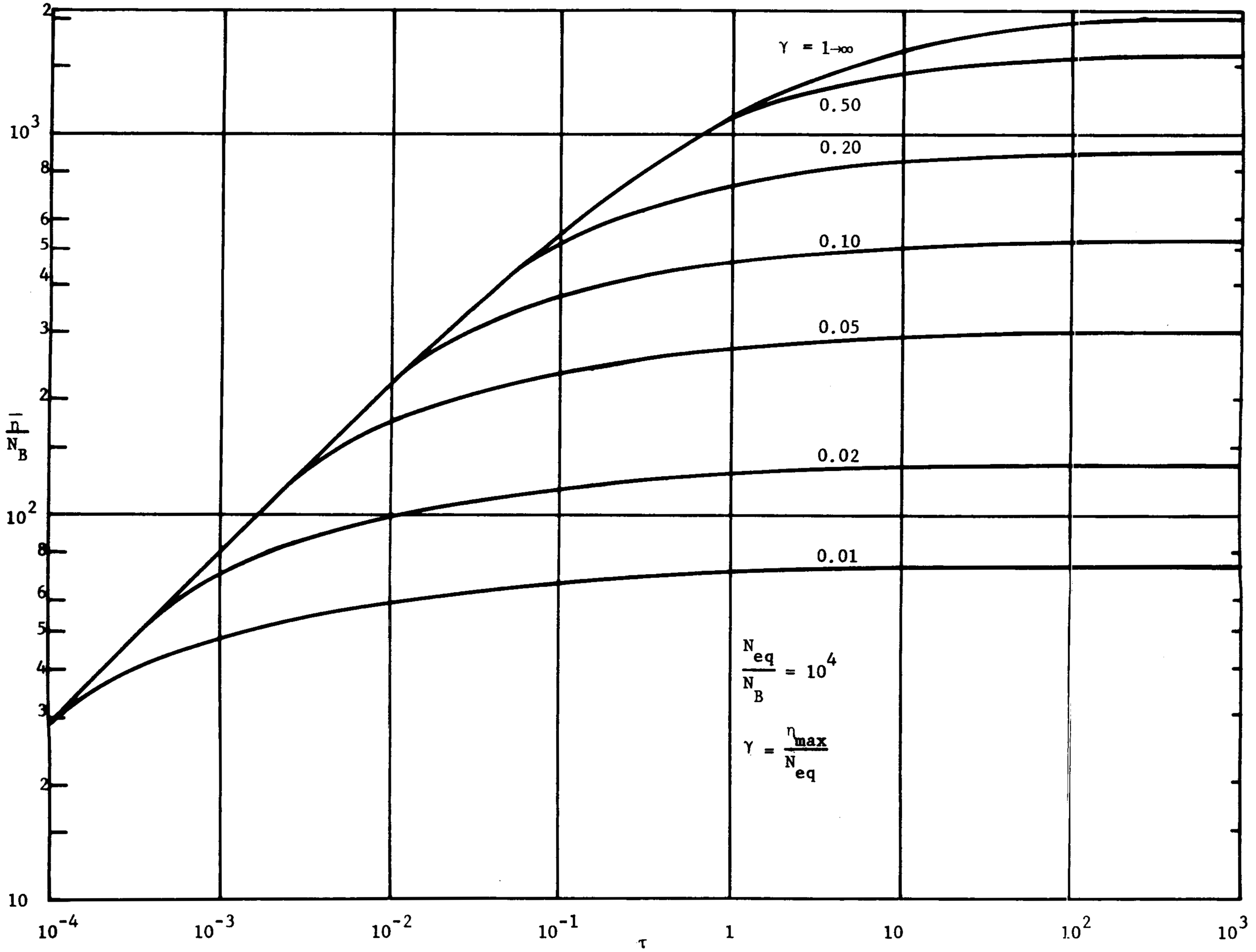

Fig. 7a. Mean ionized impurity concentration vs generalized time of diffusion predicted by the Truncated Smits Model.

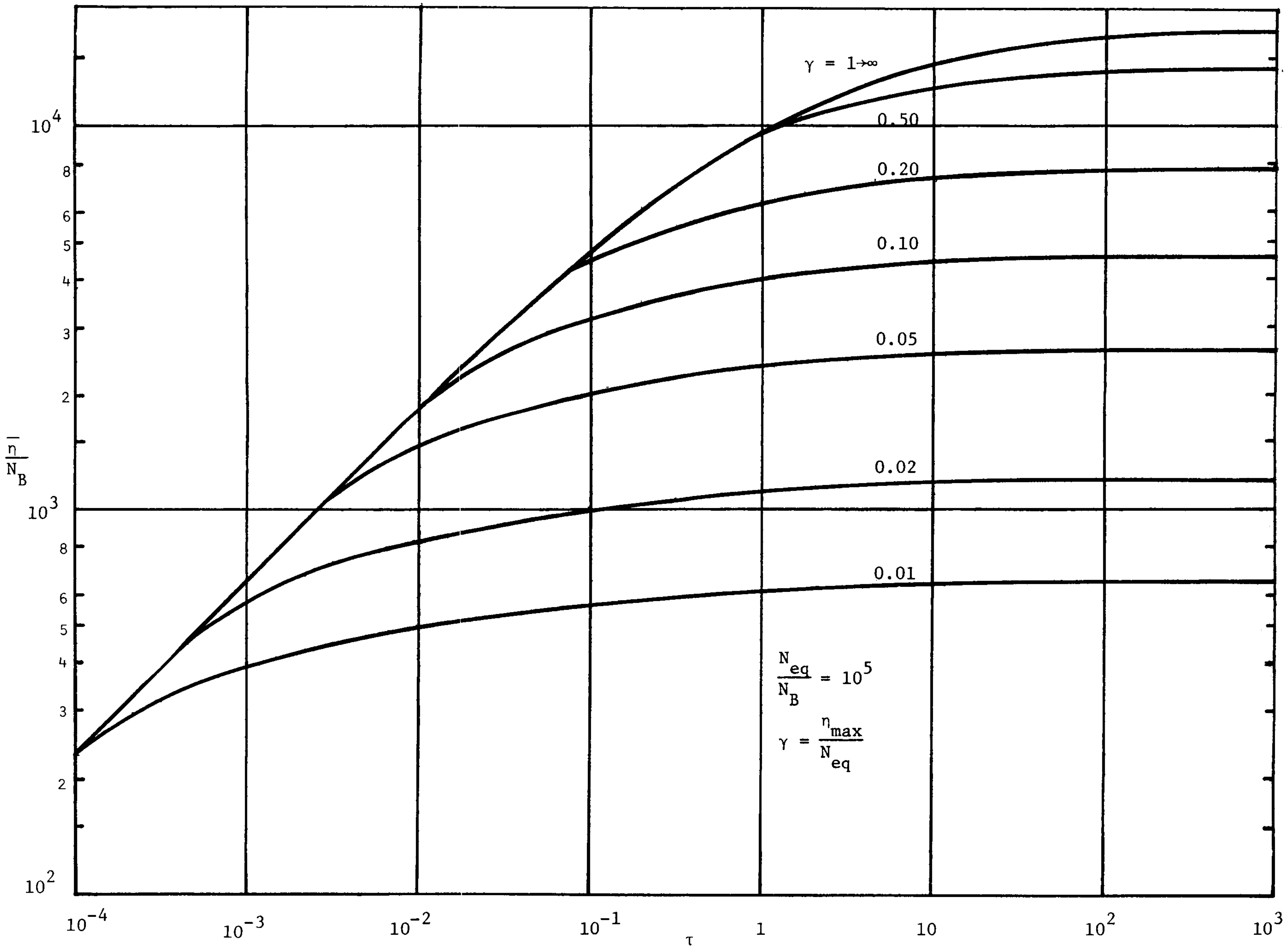

Fig. 7b. Mean ionized impurity concentration vs generalized time of diffusion predicted by the Truncated Smits model

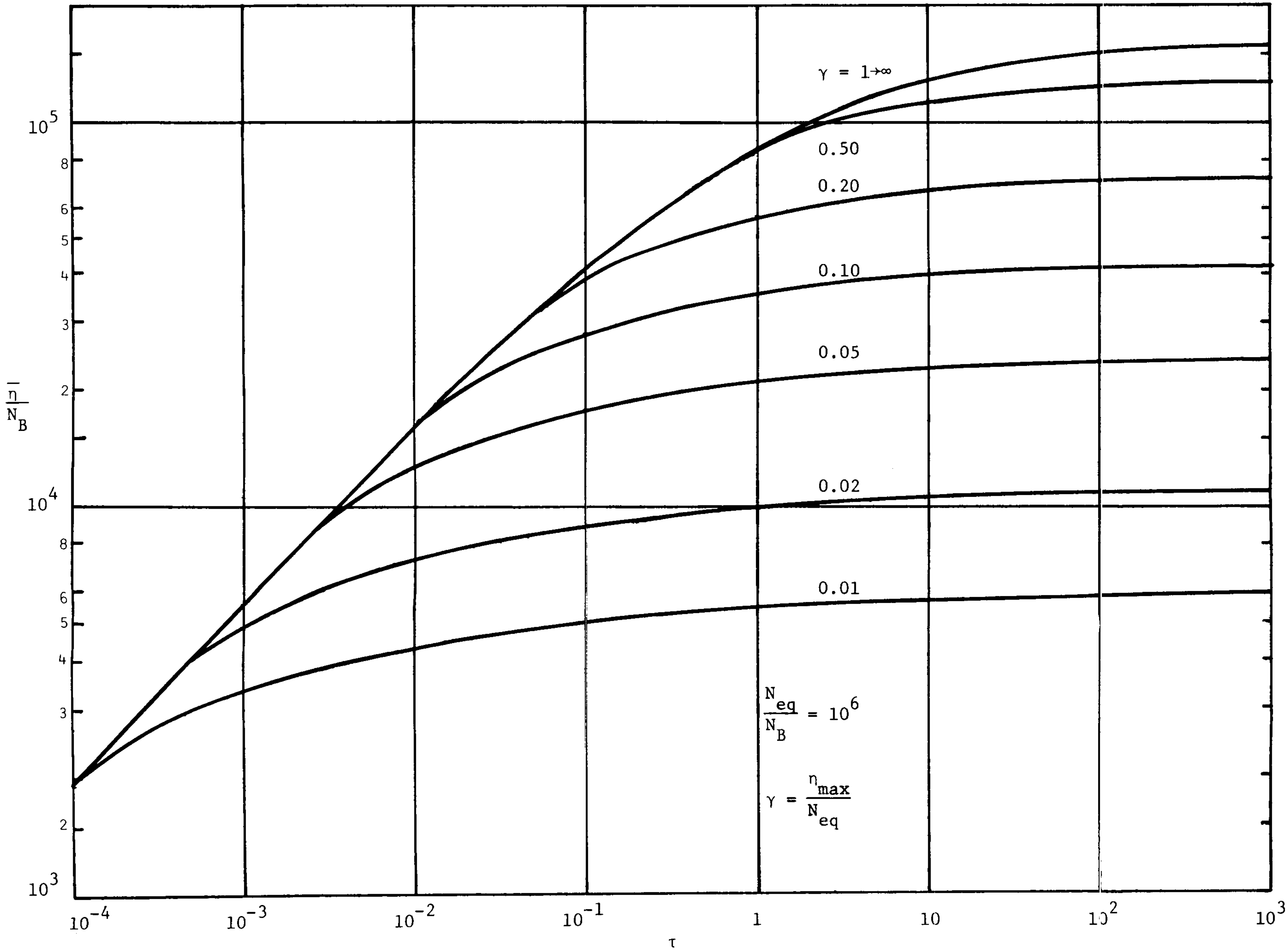

Fig. 7c. Mean ionized impurity concentration vs generalized time of diffusion predicted bt the Truncated Smits model

3. Experimental Procedures

Two different gas induction systems were employed in the course of these experiments. The first was the same as that described in Ref. 1. It was a double dilution system, operating from a 1.3% phosphine in argon source. All flowmeters were of the Rotameter type. Concentrations lower than about 100 ppm required the use of double dilution and therefore the venting overboard of some phosphine. Most of the data to be reported were gathered with this system.

3.1 Improved Gas Induction System

An improved induction system was incorporated toward the end of the contract and is diagrammed in Fig. 8. The modified system contains fewer elements, no need for overboarding, the capability of operating at a total flow rate of up to 5 ℓ/min as well as superior metering of the impurity flow. The Hastings Mass flowmeter is a transducer which measures gas flow rate by translating the temperature drop of a heated thermocouple into mass flow and thence to volume flow by appropriate conversions. The temperature is displayed on a calibrated dial or as a dc voltage

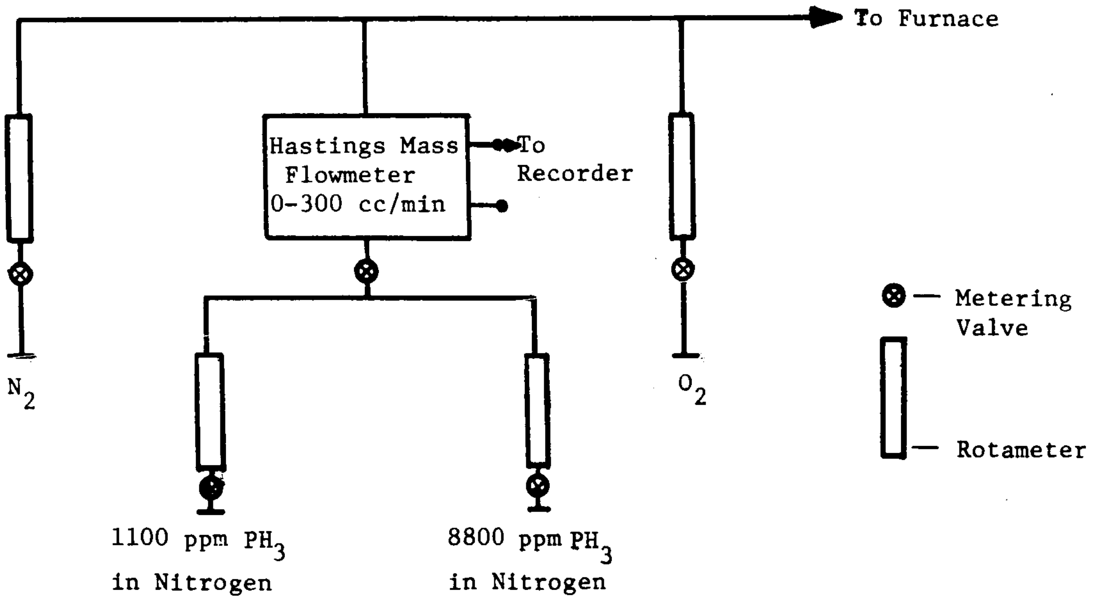

Fig. 8. Modified gas induction system

output which can be recorded. The temperature in the meter at zero flow is ~225°C. This temperature was felt to be sufficiently below the decomposition temperature of phosphine to operate satisfactorily. No evidence of phosphine decomposition in the transducer has been noted as yet.

Two different source strengths of phosphine are used in this induction system: (1) the highest available commercially (nominally 1%); (2) a source which is about an order-of-magnitude more dilute. The specific concentrations employed at present are 8800 ppm for the full strength source and 1100 ppm for the diluted source. These concentrations are by volume of phosphine in nitrogen. At a constant total gas flow through the furnace of 4 ℓ/min, the concentration of phosphine in the gas flow can be varied from 1.4 ppm to 660 ppm (vol/vol) using the Hastings Mass Flowmeter. For phosphine concentrations above 660 ppm, the mass flow meter is off scale and the Rotameters become the primary measure of impurity flow. The maximum concentration possible is ~8800 ppm which consists of undiluted flow from the high concentration phosphine tank. Oxygen flow is, of course, added but makes a negligible contribution to the total flow. For the diffusions performed at a total flow of 4 ℓ/min, the oxygen flow is held fixed at 0.028 ℓ/min.

3.2 Inductions System Performance

An analysis of variance was performed to contrast the two induction systems. In this experiment the midpoint of the tTc matrix (t = 30 min, T = 1150°C, c = 250 ppm) was repeated in five successive diffusion runs consisting of two wafers each. All wafers came from the same ingot. One of the two wafers was placed at the front of the diffusion boat; the other, at the back (the back position is downstream of the front position). During diffusion the wafers stand vertically on an edge with the wafer surface parallel to the center line of the furnace tube.

The side of the furnace tube (right or left) faced by the patterned side of the wafer was varied to make four runs. The fifth was a repeat of the fourth, making the runs as follows:

1 $\left\{\begin{matrix} F & R \\ B & R \end{matrix}\right\}$

2 $\left\{\begin{matrix} F & L \\ B & L \end{matrix}\right\}$

3 $\left\{\begin{matrix} F & R \\ B & L \end{matrix}\right\}$

4 $\left\{\begin{matrix} F & L \\ B & R \end{matrix}\right\}$

5 $\left\{\begin{matrix} F & L \\ B & R \end{matrix}\right\}$

where F and B describe the wafer position with respect to the boat, L and R describe the direction in which the patterned surface of the wafer is facing (as viewed from the loading end of the furnace tube). The mean resistivity of each wafer was taken as the average of eight separate four-point probe readings on the unpatterned side of the wafer. No measurements were rejected. The overall mean sheet resistivity of the ten wafers was compared with a similar run of 10 wafers performed several weeks later. This same procedure was followed using both the old and the new induction systems. The results of the analysis are summarized in Table 1 (old induction system) and Table 2 (new system). Sheet resistivity measurements

Table 1

Table of means using old induction system--sheet resistivity (ohms/square)

Position	Run 1			Run 2
	Initial Hydrophobic Surface	Additional 5 min soak in 48% HF	Additional 55 min soak in 48% HF	
FR	3.77	3.84	4.06	4.04
BR	3.52	3.66	3.80	4.07
FL	3.70	3.89	3.99	4.20
BL	3.13	3.53	4.13	4.30

were also made after soaking the wafers for various lengths of time in concentrated commercial hydrofluoric acid (HF). The purpose of these measurements was to assess the importance of the observations reported by Baird (Ref. 6) and to alter the present measuring procedure if warranted. Baird reported a dependence of sheet resistivity upon post diffusion chemical treatments--specifically sheet resistivity changed with HF soak time. As shown in Table 1, a significant change with time of HF soak was observed. The direction of the change is towards higher values of sheet resistivity, as though some surface contribution to the sheet resistivity measurement is being removed by the HF soak.

Table 2

Table of means using new induction system--sheet resistivity (ohm/square)

Position	Run 1	Run 2
FR	3.24	3.70
BR	3.27	3.31
FL	3.28	3.45
BL	3.19	3.14

While a significant change in resistivity is noted during such a treatment, other factors have an equally pronounced effect, such as position on the boat, left or right facing. The most important factor on the wafers diffused with the old induction system is the variation between the resistivity means of the two runs. This variation far outweighs all the other factors in importance. The apparent elimination of this variation using the new induction system suggests that a significant improvement in reproducibility has been achieved. This conclusion is tentative since it is based on only two runs. Repetition of the same point and perhaps others is necessary before this conclusion can be stated without reservations.

All diffusions of this contract (with the exception of those used in the analysis of variance just described) were carried out using the old induction system.

3.3 Measurement Techniques

The measurement of the intermediate diffusion parameters, junction depth and sheet resistivity, were accomplished using the procedures described in Ref. 1 with several exceptions:

1. Sheet resistivity measurements, while taken on both the patterned and unpatterned sides of the wafer, were used only from the unpatterned for the analysis.
2. The number of junction depth measurements was increased to 9 (4 on the patterned side of the wafer, 5 on the unpatterned side). In addition each region delineated was photographed using the 5350 A line of thallium. The junction depth was determined by counting the fringes of the photomicrographs. Figures 9a and 9b show a typical set of such photomicrographs. The variation in junction depth from the patterned side of the wafer to the unpatterned side is less than 10%. For practically all the wafers the median number of fringes is the same whether all nine positions are considered or whether only the five positions on the unpatterned side are considered (positions 5-9). Over most of the measuring range, values are accurate only to the nearest fringe, the primary limitation being the ability to distinguish the point on the fringe pattern coinciding with the junction. The intersection of the top surface with the groove is well defined by the abrupt change in direction of the fringes.
3. Each diffusion run consisted of two wafers--one on the upstream end of the boat, the other on the downstream end. Each wafer was evaluated independently of the other and incorporated into the analysis as an independent point.

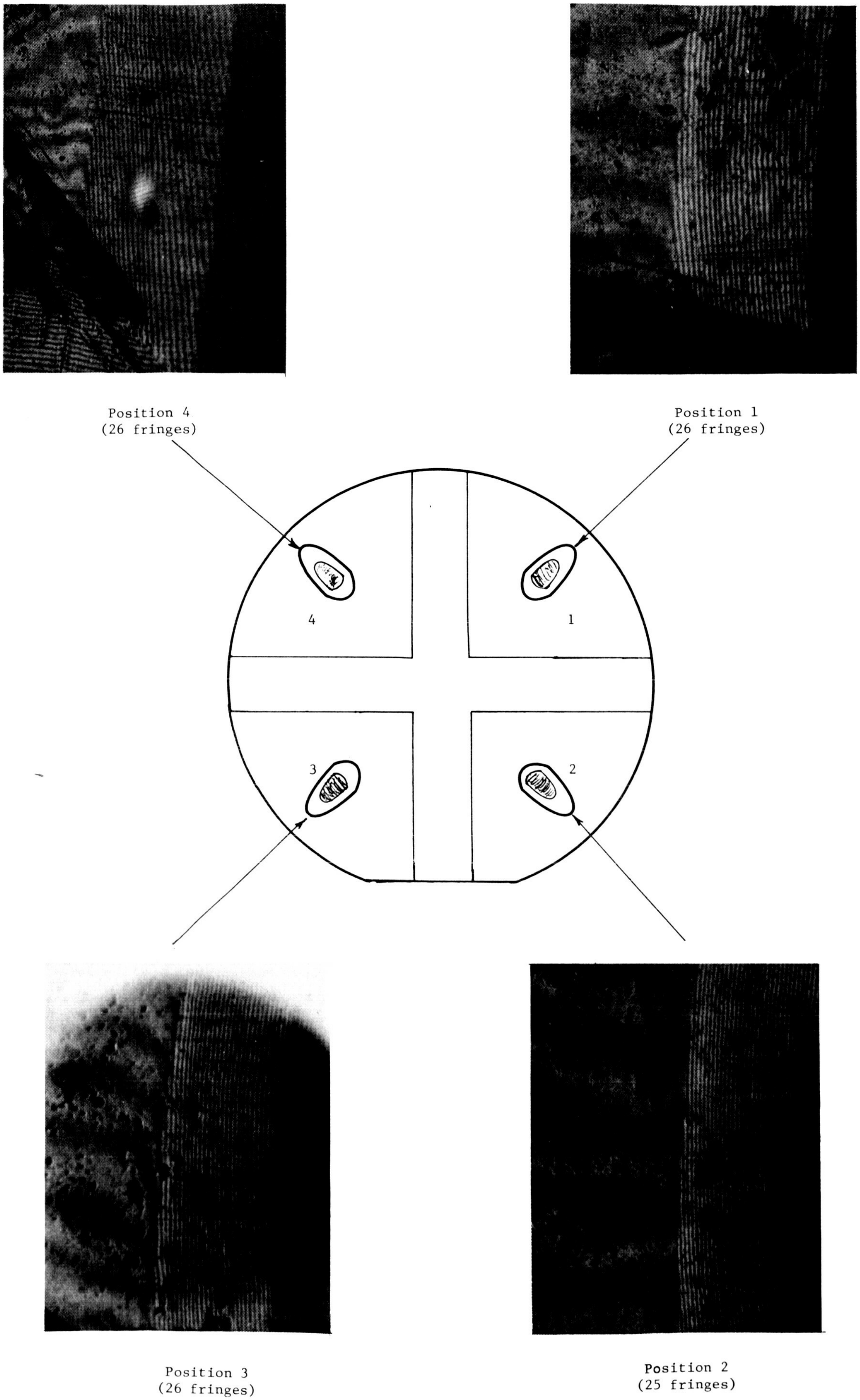

Fig. 9a. Measurements of junction depth on Patterned side of wafer

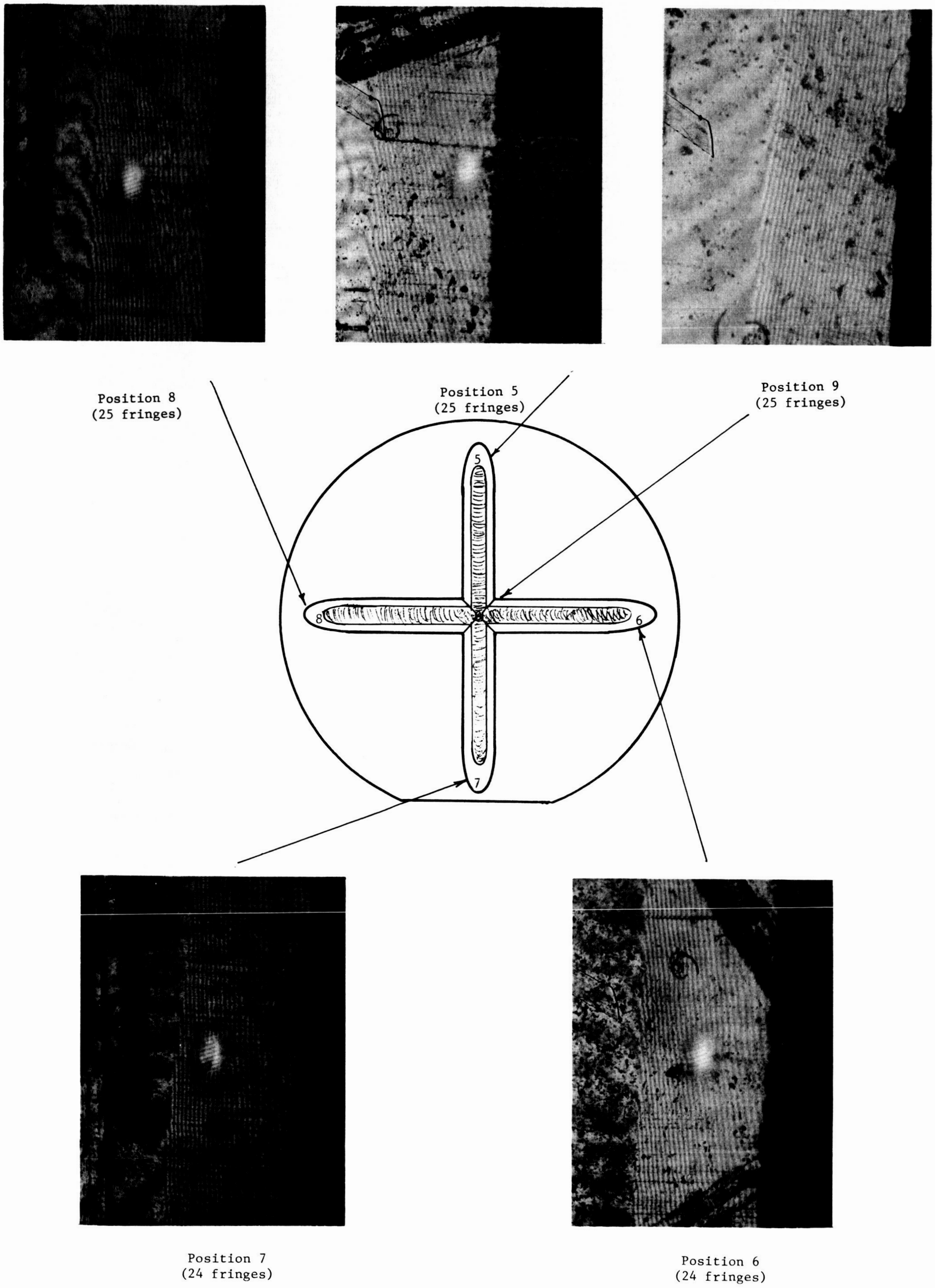

Fig. 9b. Measurements of junction depth on Unpatterned side of wafer

As before, sheet resistivity readings were made with the Texas Instruments' ρ-meter, model 635B. Junction I-V characteristics were either photographed on the Tektronix curve tracer or plotted on an x-y recorder using the following arrangement:

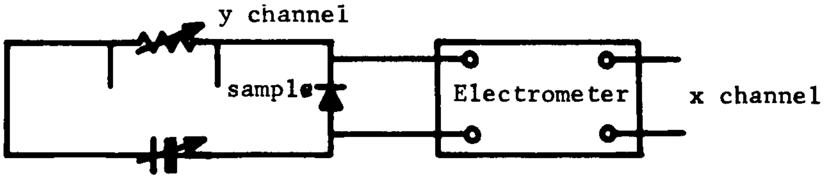

All reverse current measurements were made with the wafer resting on a hot plate kept at 175°C.

C-V plots were photographed from an oscilloscope display using the following circuit:

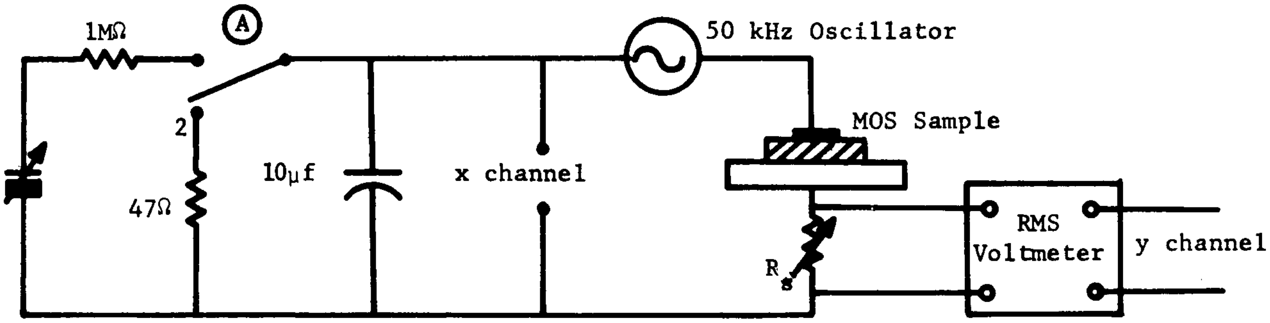

The sweep employed was not linear but was reproducible for a given dc voltage step (applied by placing switch A in position 1). The output voltage developed across a 10 μf capacitor was used as an external drive for an oscilloscope display and at the same time used to apply a slowly varying dc bias to the MOS (Metal-Oxide-Silicon) Structure (see Fig. 18). Superimposed on the dc voltage was a small 50 k Hz signal generated by an audio oscillator. The MOS device constitutes the primary ac impedance of the circuit so that the rms voltage developed across the resistor R_S depends directly on the capacitance of the MOS structure. The output of an RMS voltmeter drives the y channel of the oscilloscope. Traces of C/C_o vs V were photographed by opening the lens of the scope camera during the sweep. From such photographs, values of the flat band voltage (V_{FB}) can be read directly.

3.4 Diode Geometry

The diode geometry employed was the same as that previously used (Ref. 1) with the following modifications:

1. An aluminum ring, deposited on top of the oxide, was inserted between the dot contacting the n-diffused layer and the cam-shaped area contacting the p-type substrate. This ring covers the p-region immediately adjacent to the diffused n-p diode and forms an MOS structure suitable for obtaining measurements of V_{FB}.

2. The variations in junction area have been doubled at each position. Seventeen positions, arranged as before, are included. Each position now consists of four circular diodes representing diameters of 4.5, 9.0, 13.5 and 18.0 mils. A photomicrograph of a completed unit is shown in Figure 10 which can be seen to be identical to the geometry previously employed (Fig. 10) with the exception of the added aluminum ring which is on top of the oxide. The aluminum ring in Fig. 10 appears darker than the aluminum contacting the silicon. This darkening appears on occasion during various annealing cycles. Its origin is not known but is presumed to result from some sort of uncontrolled contamination originating during evaporation, photoengraving, or annealing. It is similar in appearance to the anion reaction technique described by Corl (Ref. 7).

3.5 Wafer Selection

The starting silicon was again chosen to be about 1 ohm-cm p-type. This resistivity corresponds to a substrate doping in the vicinity of 2×10^{16} cm^{-3}. From Fig. 68 of Ref. 8 (reproduced here as Fig. 11) the calculated value of pinch-off voltage is seen to be quite sensitive to substrate doping level (as well as oxide thickness). For a surface state charge density of 5×10^{11} cm^{-2}, a typical

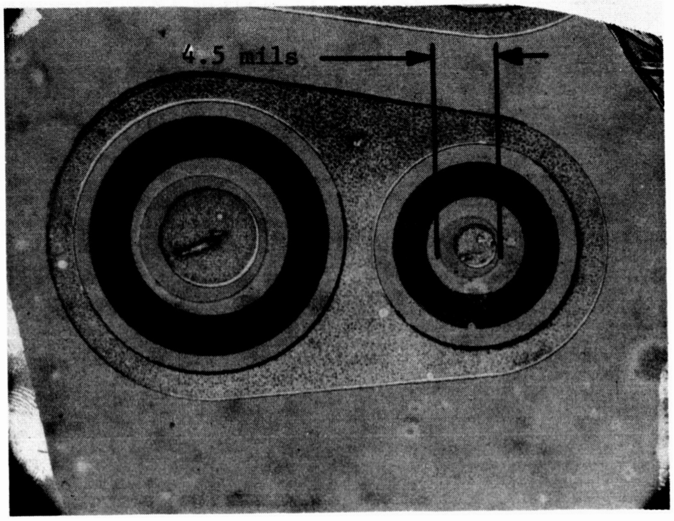

a. Present

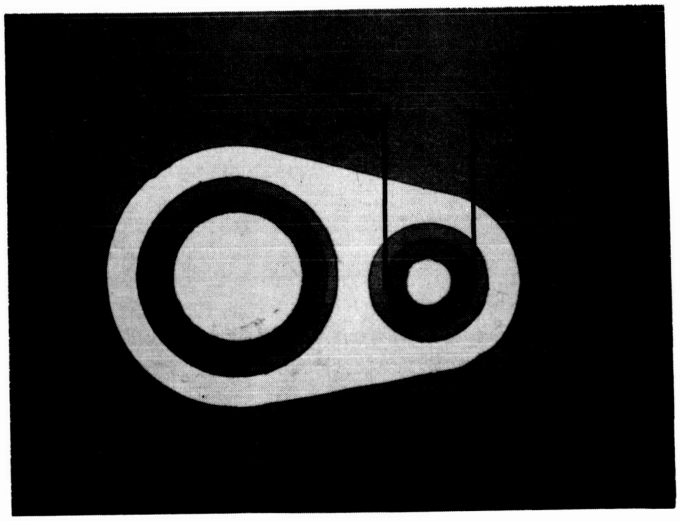

b. Previous

Fig. 10. Diode geometry

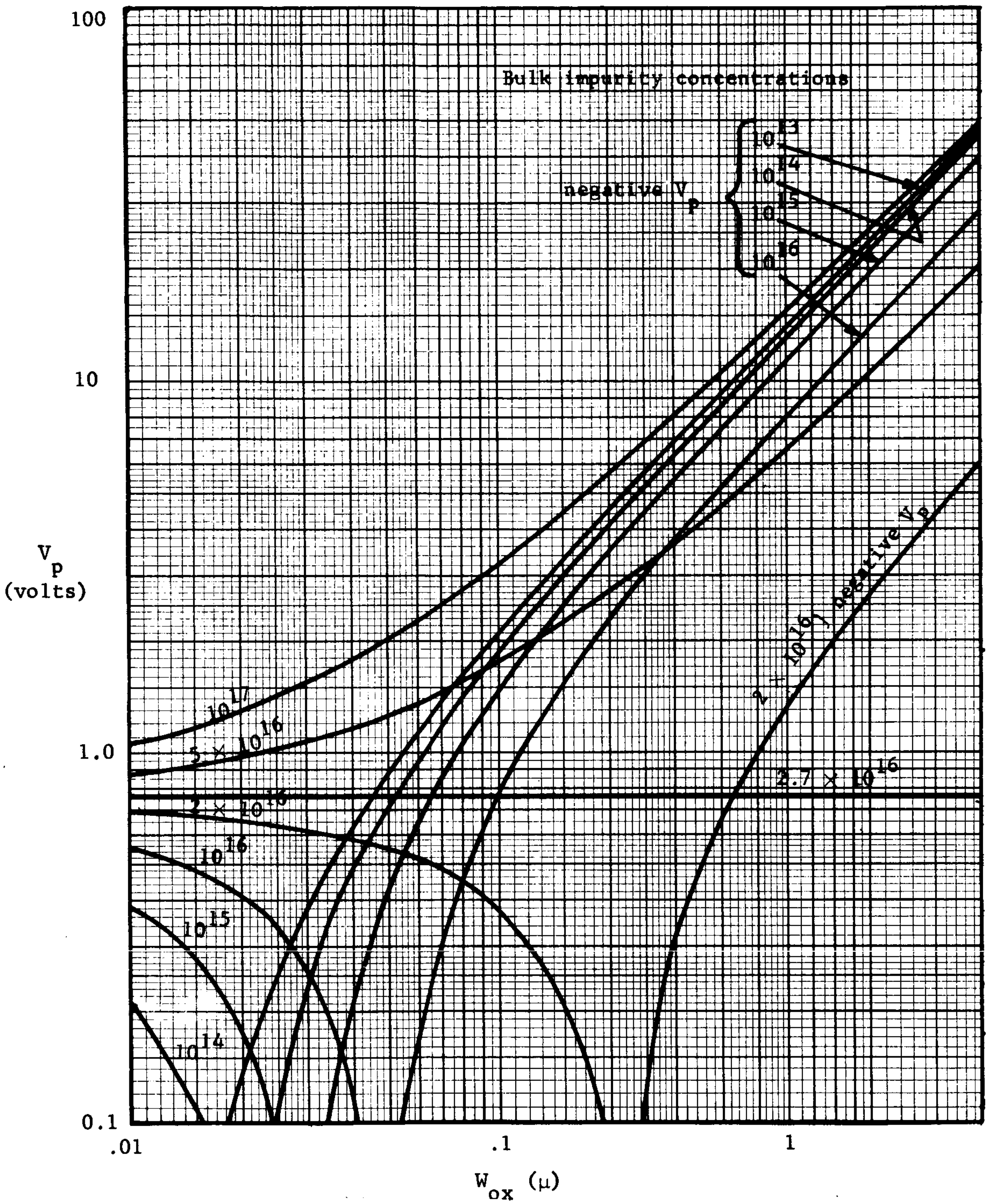

Fig. 11. V_p for an n-type field induced surface channel with a positive surface state charge density of $5 \times 10^{11}/cm^2$ (W_{ox} = oxide thickness; V_p = pinch off voltage).

value reported following thermal oxidation, the pinch-off voltage is most sensitive to substrate doping in the vicinity of 2×10^{16} cm^{-3}. Both positive and negative values of pinch off voltage are possible. At substrate impurity concentrations much greater than 2×10^{16}, the charge incorporated into the oxide is not sufficient to produce a built-in inversion layer; below this value, the surface generally does contain such an inversion layer. Around 2×10^{16} cm^{-3} small variations in the oxide charge can cause a large change in such surface electrical properties as inversion layer formation. Consequently, the observed I-V characteristics of planar diodes should also reflect the influence of substrate doping upon inversion layer formation. This influence is illustrated in Fig. 12 which compares the reverse currents of diodes on wafers that were diffused identically but with different substrate resistivities. The extreme sensitivity of the 1 ohm-cm substrate to typical surface conditions is manifested by the relatively large scatter in the reverse currents of the various diodes as compared with either the 0.06 ohm-cm substrates ($\sim 10^{18}$ cm^{-3}) or the 10 ohm-cm substrates ($\sim 10^{15}$ cm^{-3}). That the grouping of the data is much better on these latter substrates reflects the fact that surface contributions are dominating the measurements. In addition the magnitude of the reverse current is much greater on the 10 ohm-cm substrate ($\sim$ 10 μa at 1 v) than on the 0.06 ohm-cm substrate ($\sim$ 0.001 μa at 1 v). This large difference can be explained most easily by a surface inversion or depletion layer contribution to relatively similar bulk properties. In this picture the spread in measured properties of the 1 ohm-cm substrates is attributed to increased sensitivity to surface contribution. For evaluating the surface contribution this substrate resistivity is preferred and has been used in these experiments.

A batch of chemically polished silicon wafers were obtained from a commercial vendor and classified according to resistivity as follows:

Resistivity (ohm-cm)	Impurity Concentration (10^{16} cm^{-3})	Quantity	Code Letter
greater than 1.2	less than 1.4	0	D
1.20 - 1.16	1.4	0	E
1.15 - 1.11	1.5	1	G
1.10 - 1.05	1.6	17	H
1.04 - 1.01	1.7	23	J
1.00 - 0.97	1.8	33	K
0.96 - 0.93	1.9	37	L
0.92 - 0.89	2.0	39	N
0.88 - 0.86	2.1	25	O
0.85 - 0.83	2.2	27	P
0.82 - 0.80	2.3	25	T
less than 0.80	greater than 2.3	12	X
	TOTAL	239	

To classify the wafers, the resistivity measurements were made at five different points on each surface of the wafer. Of the 10 values measured, the fifth highest was used to classify it. The other nine readings were generally within ± 10% of this value. The specification for the dislocation density of these wafers was less than 500 etch pits/cm^2.

Wafers selected from the most populous groups for diffusion were processed as listed in Appendix B.

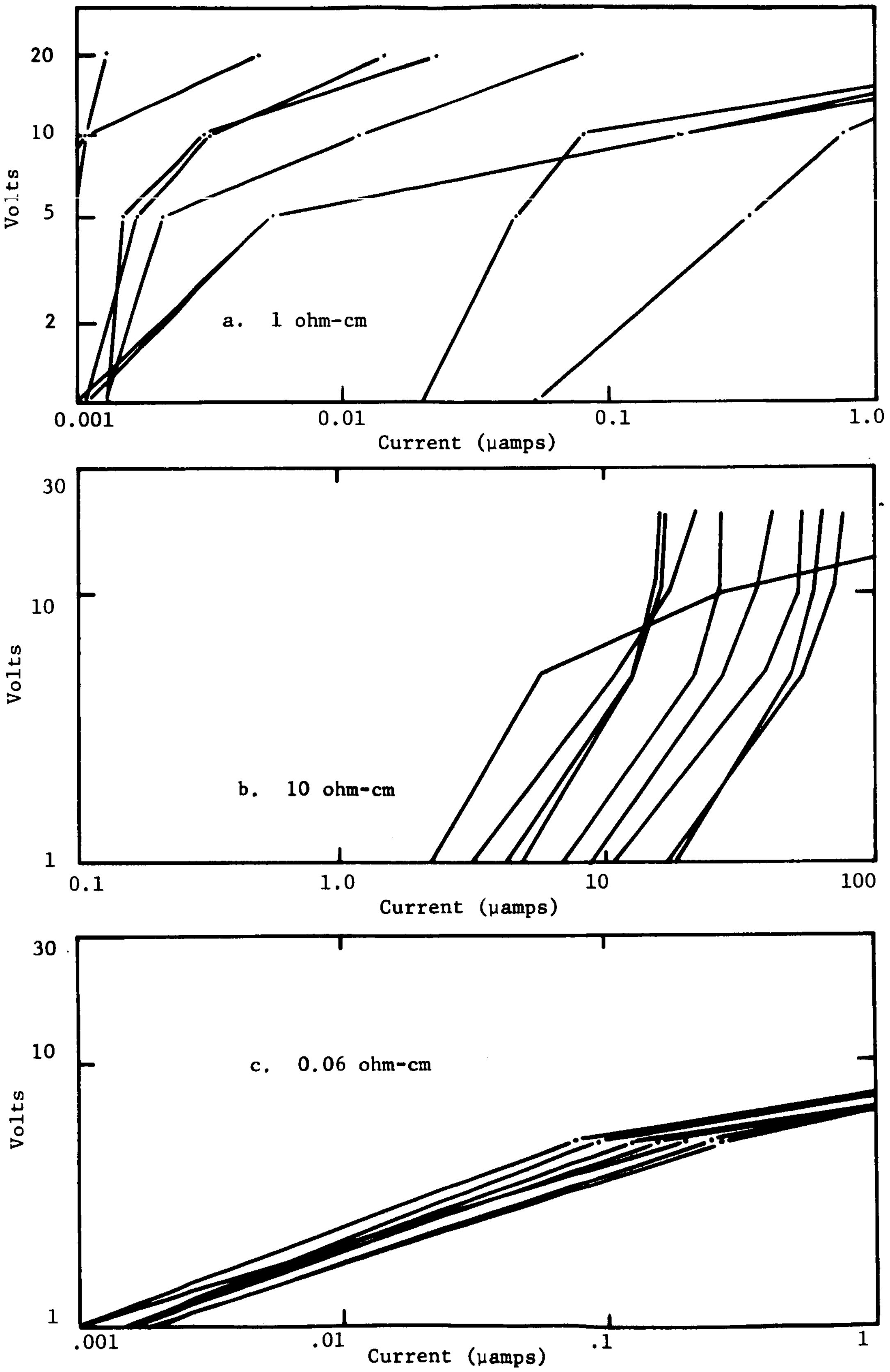

Fig. 12. The influence of substrate doping upon junction reverse current. (Each separate curve is a different diode; the junction areas are all the same.)

4. Evaluation of the Truncated Smits Model

Copies of the data sheets developed in the course of performing the matrix diffusion experiment are reproduced in Appendix C. These worksheets show: (1) the values of independent variables time (t), temperature (T), and phosphine concentration (c); (2) the measured values of intermediate diffusion parameters, sheet resistivity (ρ_s) and junction depth (x_j); (3) the calculated values of average resistivity $\bar{\rho}$ and average net impurity concentration $\bar{\eta}$. The units of each column are indicated (in one of the junction depth columns f means number of thallium fringes).

Two sets of plots have been made from these data. In Fig. 13, junction depth is plotted against time. Each separate figure is for a constant temperature; phosphine concentration during diffusion is the parameter varied. The shape of these curves as predicted by the truncated Smits model (Eqs. 2 - 8) is drawn in Fig. 6 for various ratios of N_{eq}/N_B. The axes are chosen as the dimensionless quantities $\xi(\equiv x_j \frac{K}{D})$ and $\tau(\equiv t \frac{K^2}{D})$ so as to retain the compact form of the Smits solution. From Eqs. 9 and 10 $\tau = B^2$ and $\xi = 2AB$. K and D are presumed to be functions of temperature only and the ratio $(\frac{K}{D})$ is thought to be relatively constant with temperature. The maximum value of N_{eq} is the limiting solid solubility, probably about 10^{21} cm^{-3} (Ref. 4), so that the largest ratio of N_{eq}/N_B expected in these experiments is on the order of 10^5. In Fig. 14 the calculated values of $\bar{\eta}/N_B$ from the model are plotted as a function of t. Again each separate plot is for a given diffusion temperature and phosphine concentration is the parameter varied within each plot. The curves predicted by the truncated Smits model are shown in Fig. 7. Three parameters must be adjusted to give the best fit of the data to the form predicted by the model: γ, τ, and N_{eq}/N_B. The best fit to the present data at 1100°C results from letting $\tau = 3$ correspond to $t = 10^3$ min and at

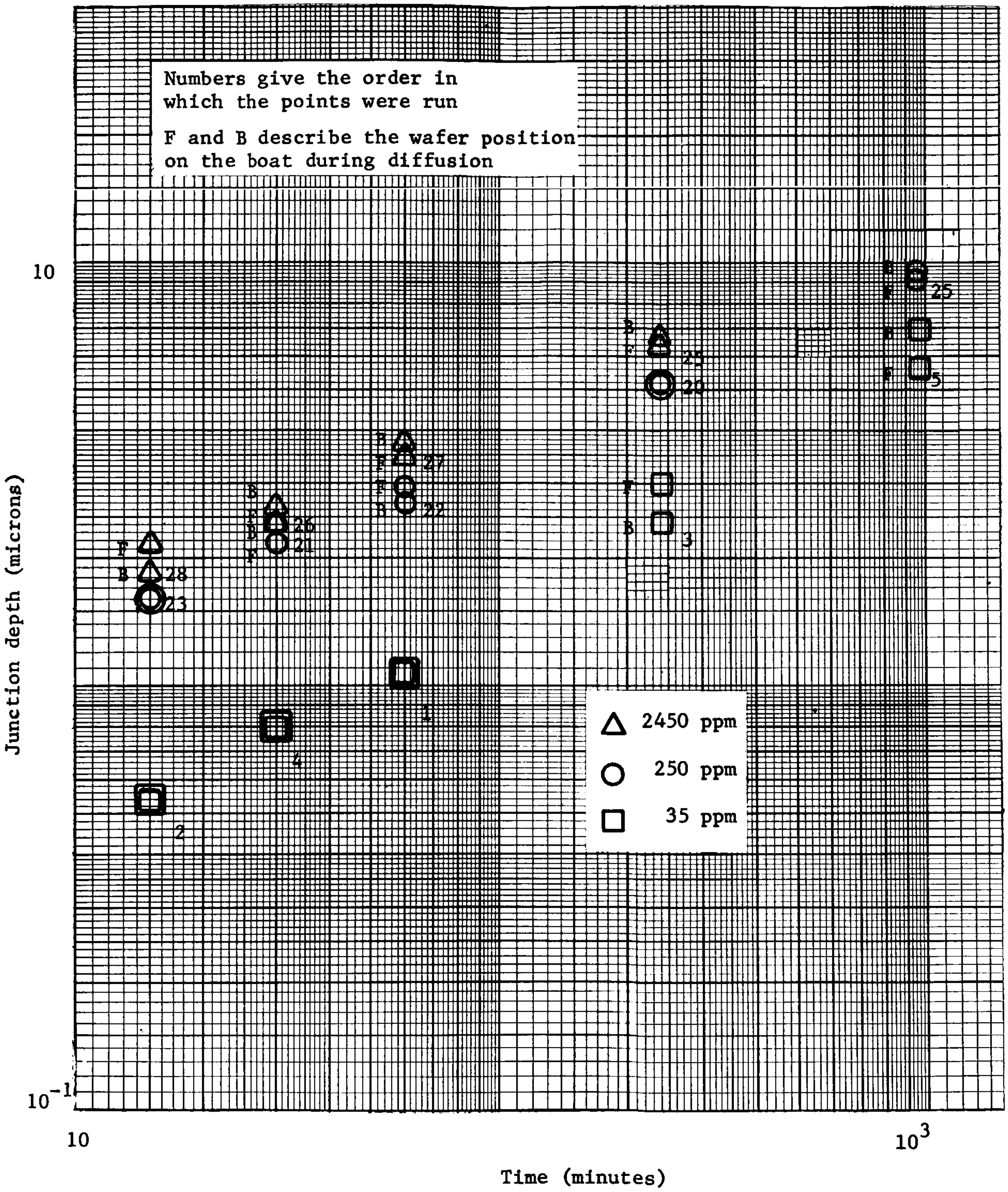

Fig. 13. Measured junction depth vs time
a. 1100°C data

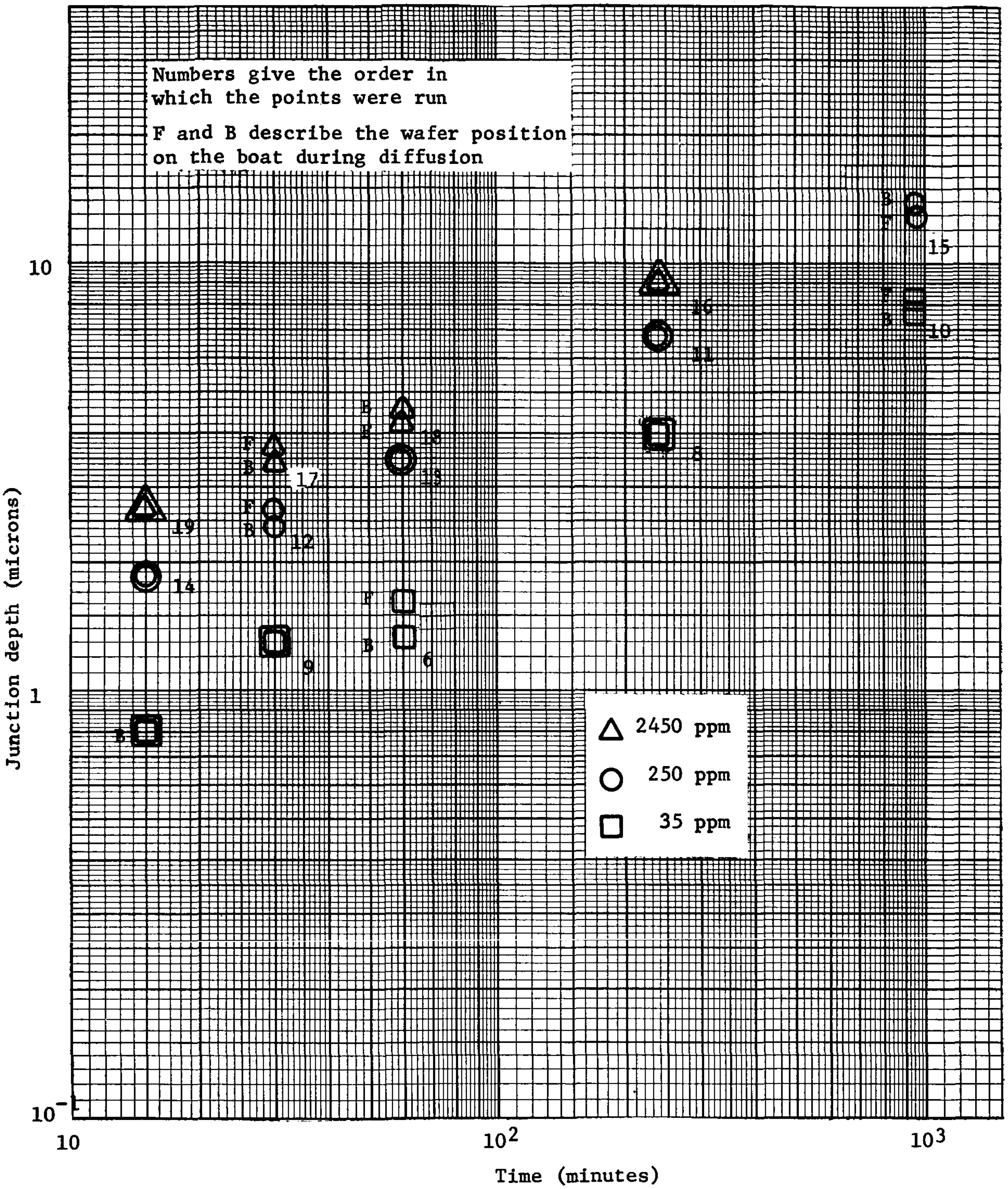

Fig. 13. Measured junction depth vs time
b. 1150°C data

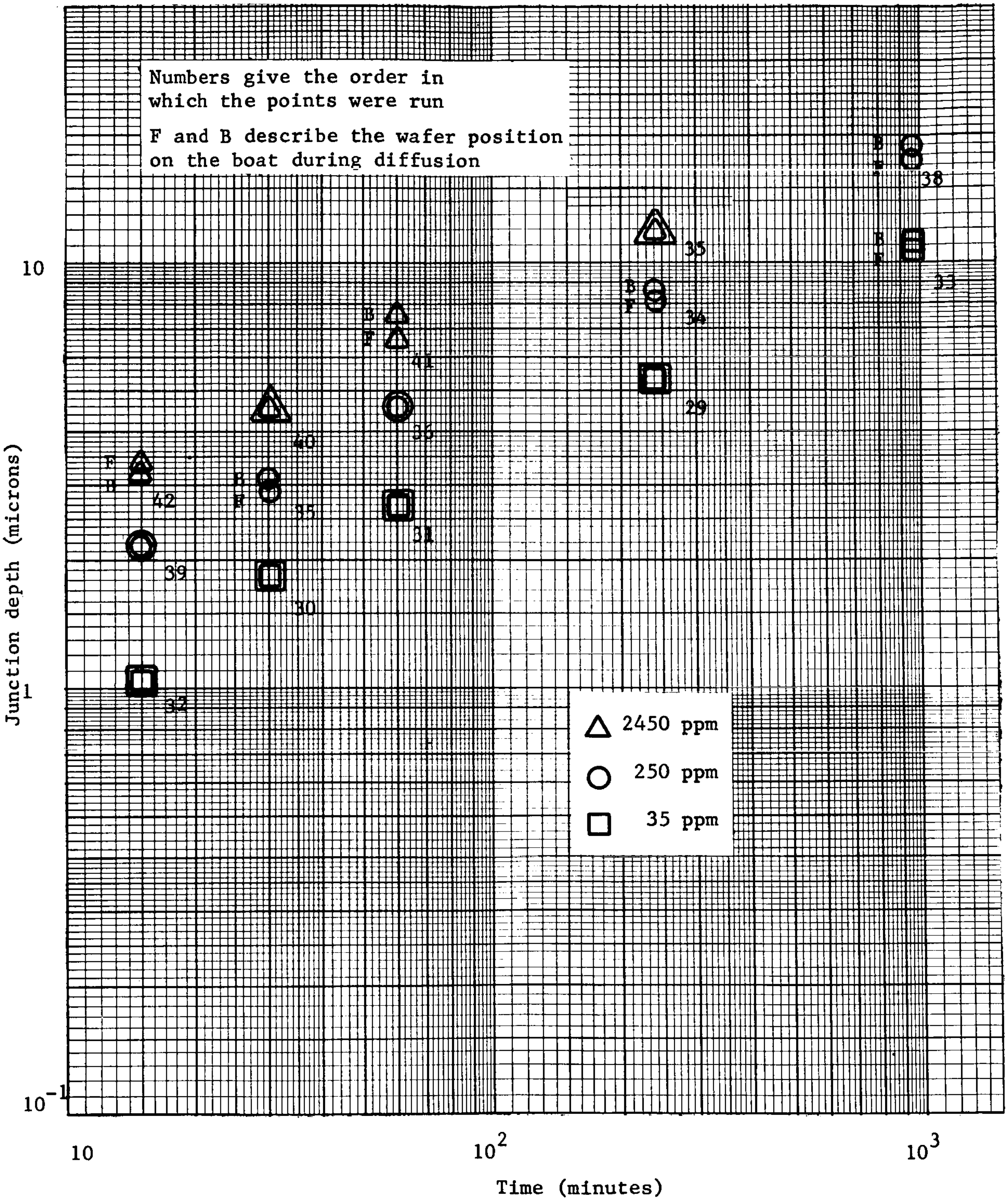

Fig. 13. Measured junction depth vs time
c. 1200°C data

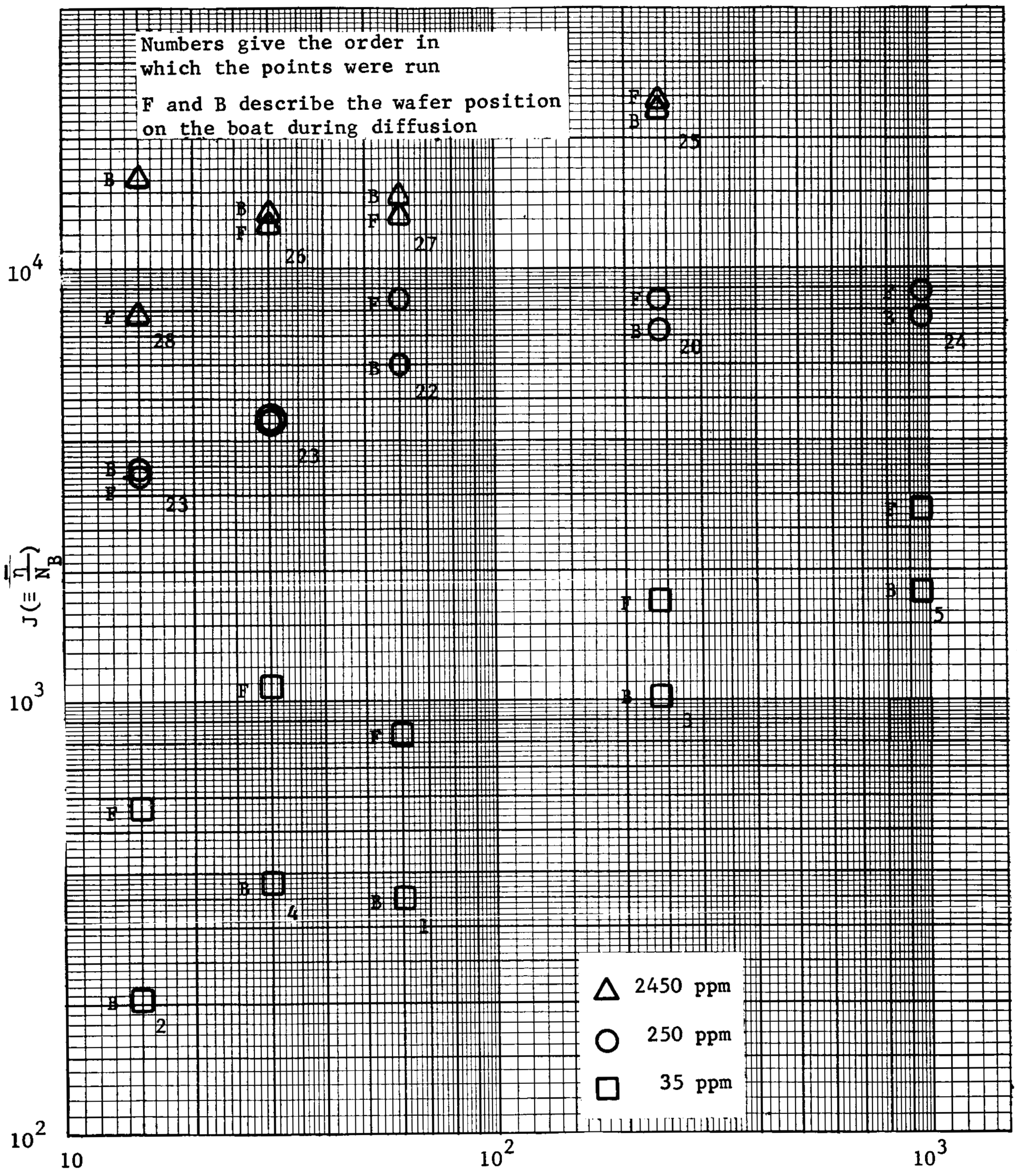

Fig. 14. Average net impurity concentration as calculated from the data, vs time
a. 1100°C data.

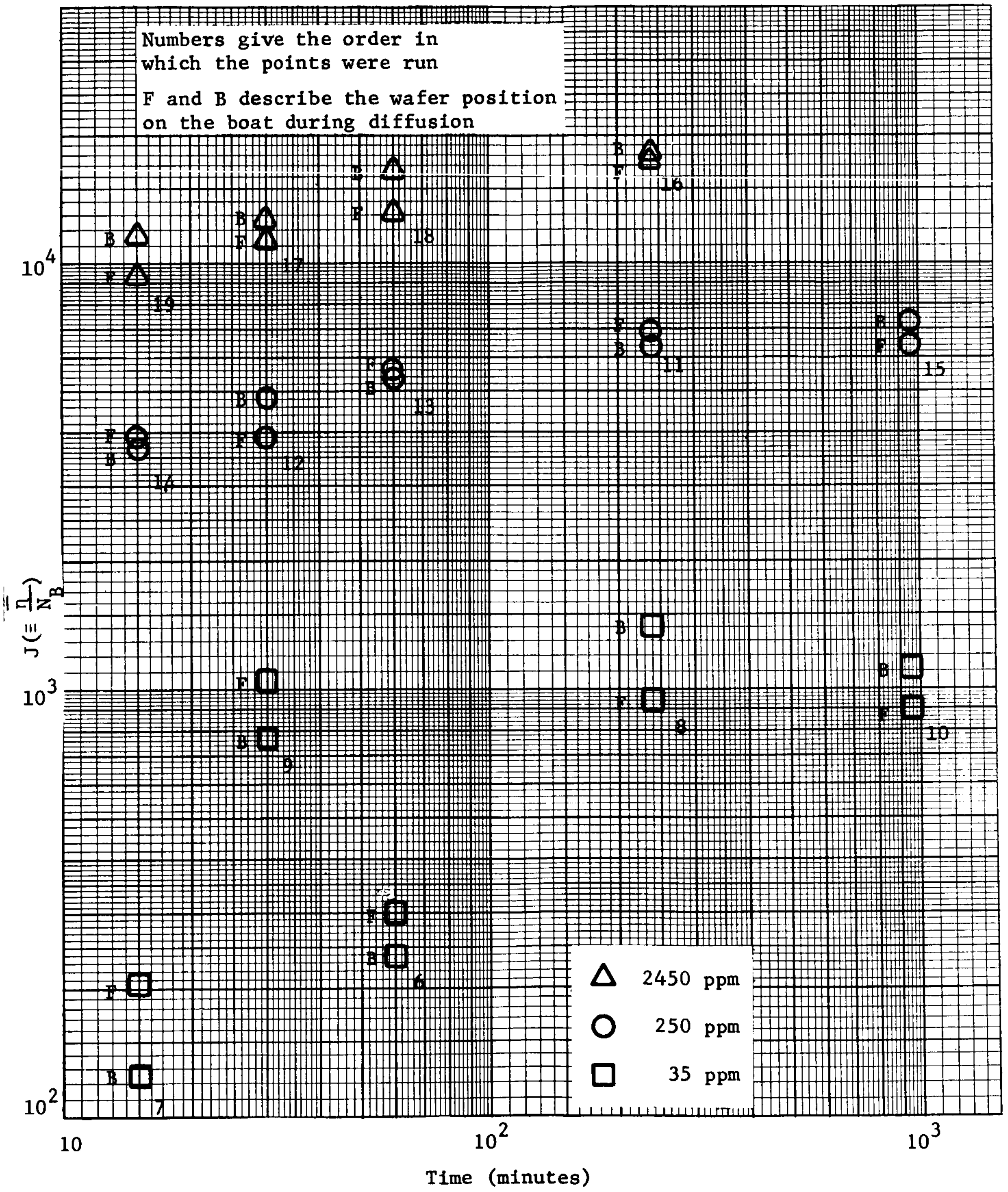

Fig. 14. Average net impurity concentration as calculated from the data, vs time
b. 1150°C data

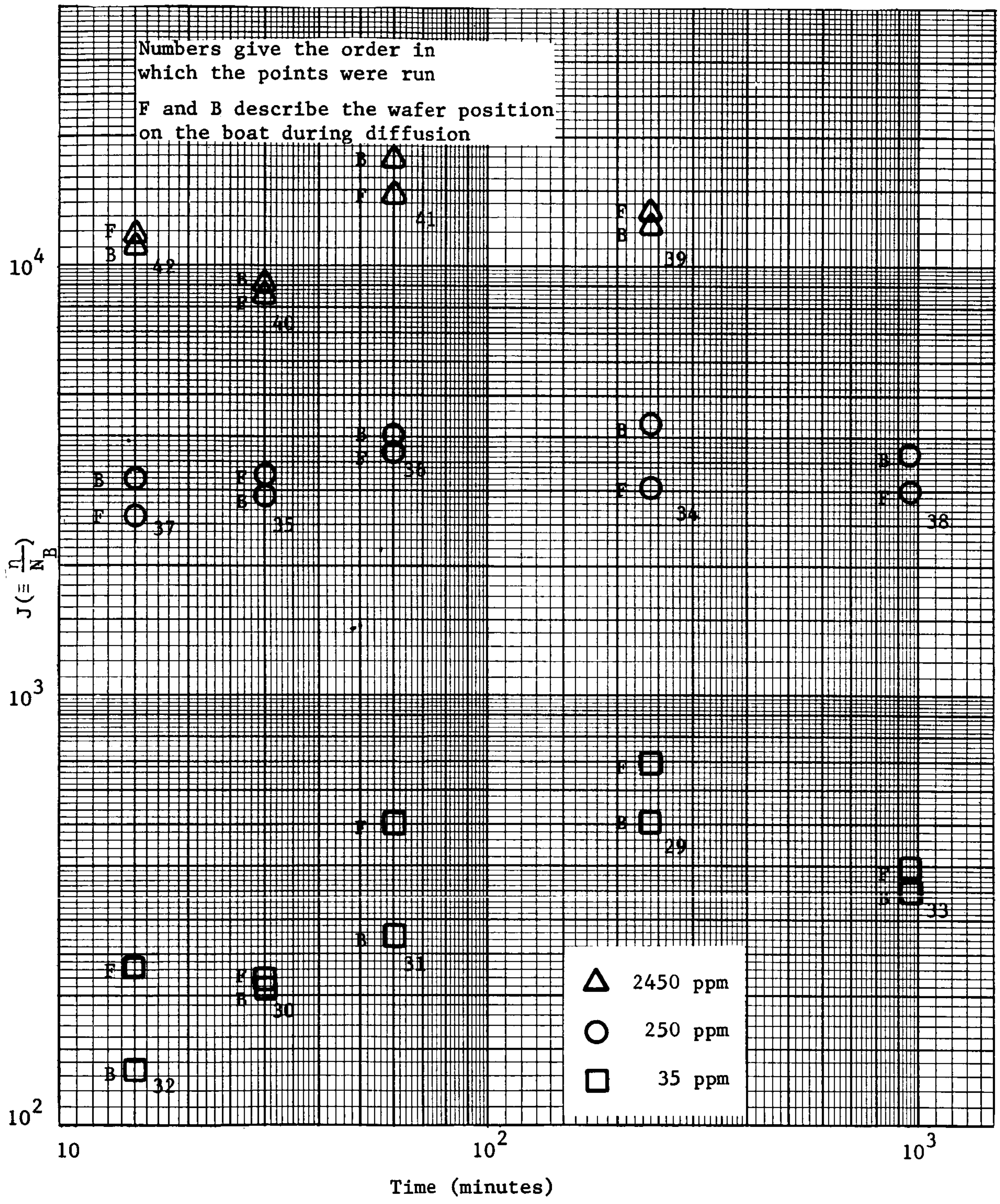

Fig. 14. Average net impurity concentration as calculated from the data, vs time
c. 1200°C data

$c = 35$ ppm $\quad \frac{N_{eq}}{N_B} = 1.3 \times 10^4 \quad \gamma = 1$

$c = 250$ ppm $\quad \frac{N_{eq}}{N_B} = 3 \times 10^4 \quad \gamma = 0.5$

$c = 2450$ ppm $\quad \frac{N_{eq}}{N_B} = 6 \times 10^5 \quad \gamma = 0.1$

Using the values of τ and $\frac{N_{eq}}{N_B}$ to enter the $\xi - \tau$ chart, the following ratios of $\frac{x_j}{\xi}$ were read off:

c(ppm)	x_j/ξ (μ)
35	0.6
250	1.4
2450	1.5

The ratio $\frac{x_j}{\xi}$ should be the same for all values of c. The departure from this prediction could be due to either experimental or conceptual inadequacies. Which is more at fault is not clear at present, although the presence of an intermediate oxide is not explicitly accounted for in the present model. The chemical reactions between the oxide and the silicon have also been ignored.

At 1150°C the best fit is obtained by letting $\tau = 10$ correspond to $t = 10^3$ min. The other two fitted parameters are:

c(ppm)	$\frac{N_{eq}}{N_B}$	γ
35	6×10^3	1.0
250	6×10^4	0.5
2450	7×10^5	0.05

By comparing the plots of junction depth (Fig. 13) and (Fig. 6) the ratios of $\frac{x_j}{\xi}$ are as follows:

c(ppm)	$\frac{x_i}{\xi}$ (μ)
35	0.5
250	0.7
2450	1.1

From Eqs. 9 and 10

$$K = \left(\frac{\tau}{t}\right)\left(\frac{x_i}{\xi}\right) \tag{11}$$

$$D = \left(\frac{\tau}{t}\right)\left(\frac{x_i}{\xi}\right)^2 \tag{12}$$

Calculated values of K and D are given in Table 3.

No data fitting was done at 1200°C.

Table 3

Calculated values of K and D

	T = 1150°C	T = 1100°C
$(\frac{\tau}{t})$	$\frac{1}{10^2}$ min	$\frac{0.3}{10^2}$ min
$\frac{x_i}{\xi}$	$\sim 0.6\ \mu$	$\sim 1\ \mu$
K	$0.6 \times 10^{-2}\ \frac{\mu}{\text{min}}$	$0.3 \times 10^{-2}\ \frac{\mu}{\text{min}}$
D	$0.36 \times 10^{-2}\ \frac{\mu^2}{\text{min}}$	$0.3 \times 10^{-2}\ \frac{\mu^2}{\text{min}}$

These values of diffusion coefficient are comparable to those published in the literature ($0.2 \times 10^{-2}\ \frac{\mu^2}{\text{min}}$ is given in Ref. 9 for phosphorus diffusion at 1150°C). At higher values of phosphine concentration the calculated diffusion coefficient is higher; and at lower values of c, it is lower, varying by a factor of 2.5 over the range of c investigated.

The estimated values of K are probably only good to within a factor of 10^2 either way, since the data do not give a clear fit for τ, $\frac{N_{eq}}{N_B}$ and γ. No other estimates of this value are known at present so that no comparison with published values can be made. Usual practice is to ignore it (Ref. 10) (this is equivalent to assuming $K \to \infty$). The data gathered here, however, suggest that K is sufficiently low to justify using the Smits model. Truncating the Smits model (Fig. 2) seems to improve the model at high values of phosphine concentration.

The slope of some of the log x_j vs log t curves (Fig. 13) is less than 0.5. This is not predicted by the model (Fig. 6). There is also an interrelated temperature dependence; that is, at 1200°C all slopes are 0.5 or greater; at 1150°C the 2450 and 250 ppm curves have slopes of 0.5 or slightly less; at 1100°C, the slopes of the 2450 and 250 ppm curves are markedly less than 0.5. The slope of the 35 ppm curve is greater than 0.5 at all three temperatures investigated.

For a given value of c, N_{eq} decreases as the temperature increases, as evidenced by the fact that the value of $\bar{\eta}/N_B$ approached by the curves of Fig. 14 decreases as the temperature increases.

Evidence for sequence effects is clearly indicated in Fig. 14 in the lowest concentrations curves at both 1100°C and 1150°C. The numbers printed beside the data points give the sequence in which the diffusion runs were performed, 1 representing the 1st run, 2 the 2nd, etc. The letters F and B, also appearing beside the data points, represent the boat position of the wafer.

At both 1100°C and 1150°C the first runs of the 35 ppm sequence were the 60 min runs followed by the 15 min runs. All these points seem to fall below the curve that might be drawn through the remaining points, the rest of which were the 240 min runs followed by the 30 min runs. When the 240 min run is the first of the sequence, as it was for the 1200°C data, this sequence effect disappears. The conclusion suggested is that the furnace tube requires a period of time in excess of 75 min to reach equilibrium with the phosphine concentration flowing through it.

These same effects can be seen in Fig. 13; at 1150°C runs 6 and 7 fall below the straight line formed from runs 8, 9, and 10. Junction depth is a much less sensitive function of the diffusion variables than sheet resistivity or $\bar{\eta}$.

5. Electrical Properties Evaluation

The major goal of the electrical properties analysis has been the identification of an intermediate process parameter suitable for evaluating the surface contribution to the observed reverse current of a planar p-n junction. The intermediate process parameters (junction depth and sheet resistivity) are descriptive of bulk properties of the planar diffused junction but have been inadequate for predicting the reverse current of the diodes fabricated in this program. Fig. 15 shows the reverse currents of diodes on two wafers diffused simultaneously. From the data sheets (Appendix C) the x_j and ρ_s values are comparable but Fig. 15 shows that the reverse currents are nevertheless drastically different.

The relationship among the reverse currents of differently sized diodes again suggests that the primary correlation is with perimeter rather than area. Diode sizes a, b, c, and d of wafer 0-21 are contrasted in Fig. 16. The variation in reverse current is much nearer the variation in perimeter than the variations in area; that is, the perimeter of "a" is 4 times that of "d" while its area is 16 times that of "d". The variation in reverse current between "a" and "d" is much nearer 4 than 16.

To incorporate the surface contribution into the model of reverse current, measurements of capacitance at different voltages were made on the MOS ring inserted between the dot and the cam (Fig. 10). The correlation between current-voltage (I-V) characteristics and capacitance-voltage (C-V) characteristics is demonstrated in Fig. 17. Low reverse current diodes (wafer K24) display capacitance minimums at relatively low voltages. Large reverse current diodes (N32) exhibit capacitance dips or minimums at large voltages. The flat band voltage (V_{FB}) is arbitrarily taken to be the displacement of the capacitance minimum from the zero voltage axis. In all measured samples, the voltage applied to the aluminum electrode is negative with respect to the voltage of the silicon. When the polarity is reversed, no change of capacitance with voltage is seen. Oxide thickness is 0.8μ for all C-V measurements.

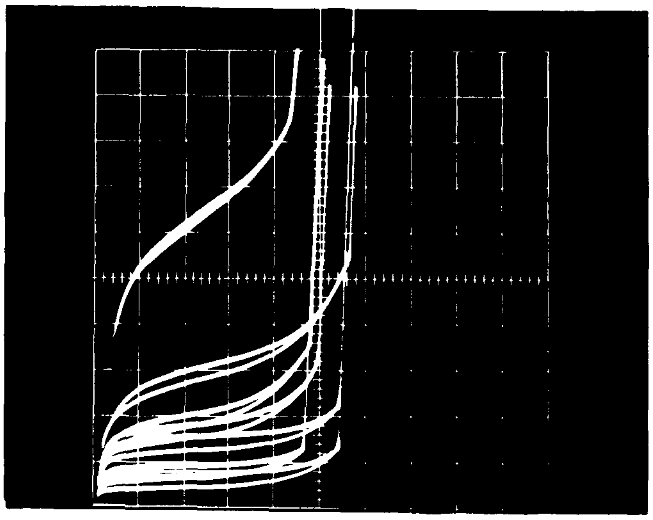

a. Wafer L25
Vertical 10 μamp/major division
Horizontal 10 v/major division

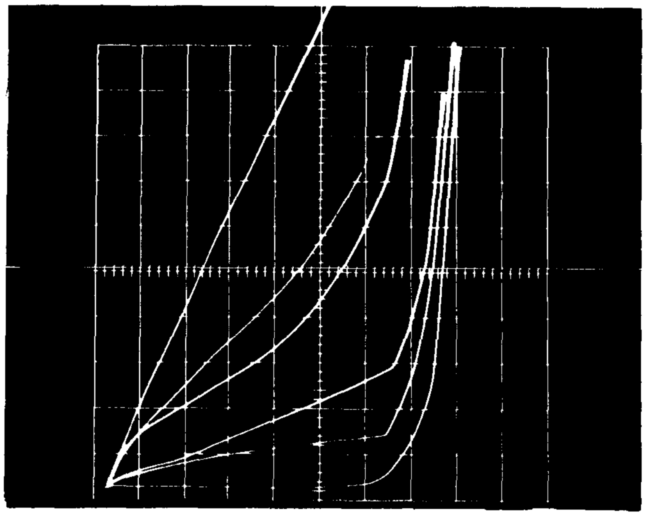

b. Wafer K23
Vertical 2 ma/major division
Horizontal 10 v/major division

Fig. 15. Diverse I-V characteristics of diodes on wafers processed simultaneously and having similar intermediate diffusion parameters. (Each curve is a separate diode characteristic on the wafer.)

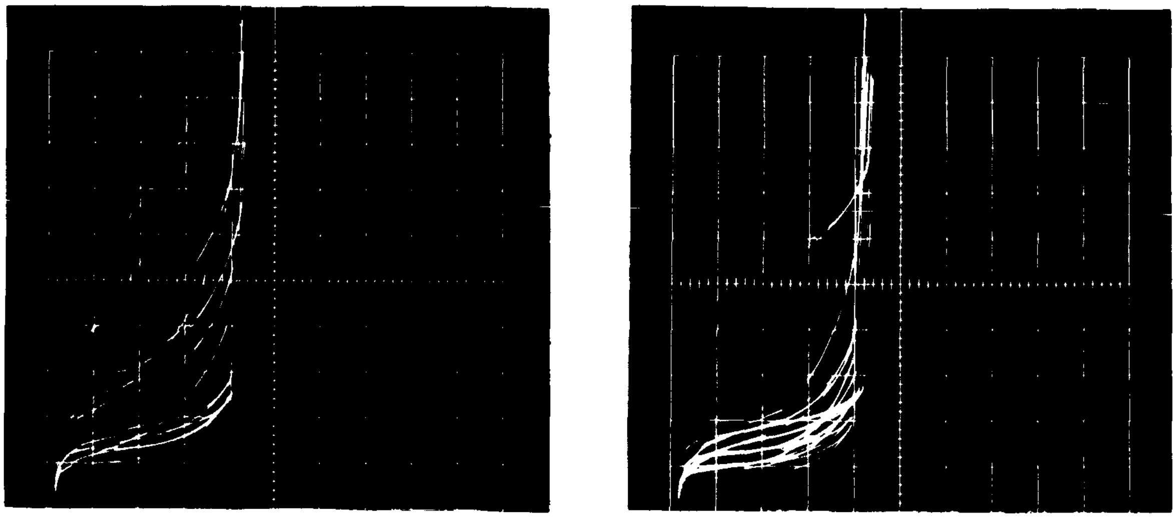

a. Wafer 0-21 a (diameter = 18 mils) b. Wafer 0-21 b (diameter = 13.5 mils)

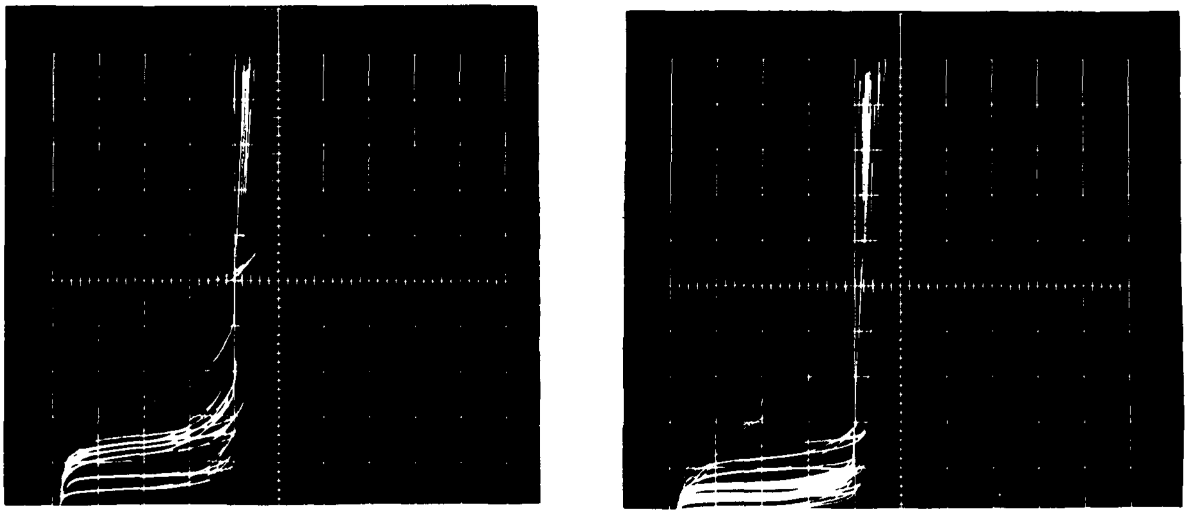

c. Wafer 0-21 c (diameter = 9 mils) d. Wafer 0-21 d (diameter = 4.5 mils)

Fig. 16. The influence of diameter upon diode reverse current. (Each curve is a separate diode characteristic on the wafer.) Temperature: 175°C; Vertical: 10 μ amp/ major division; Horizontal: 10 v / major division

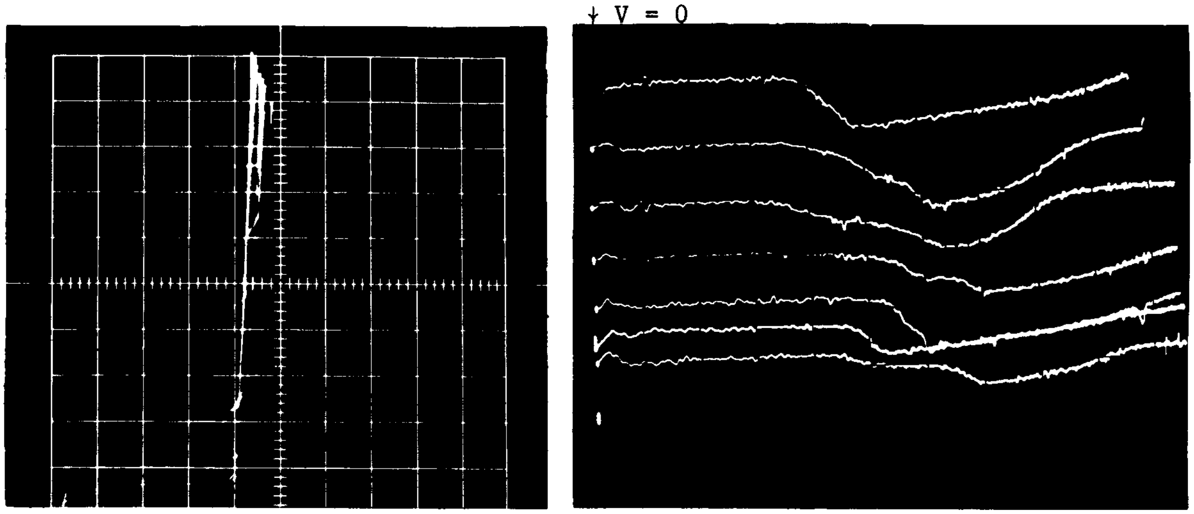

a. I-V Characteristics
Vertical 50 μ amps/major division
Horizontal 10 v/major division

b. C-V Characteristics
Vertical C/C_o
Horizontal 20 v/major division

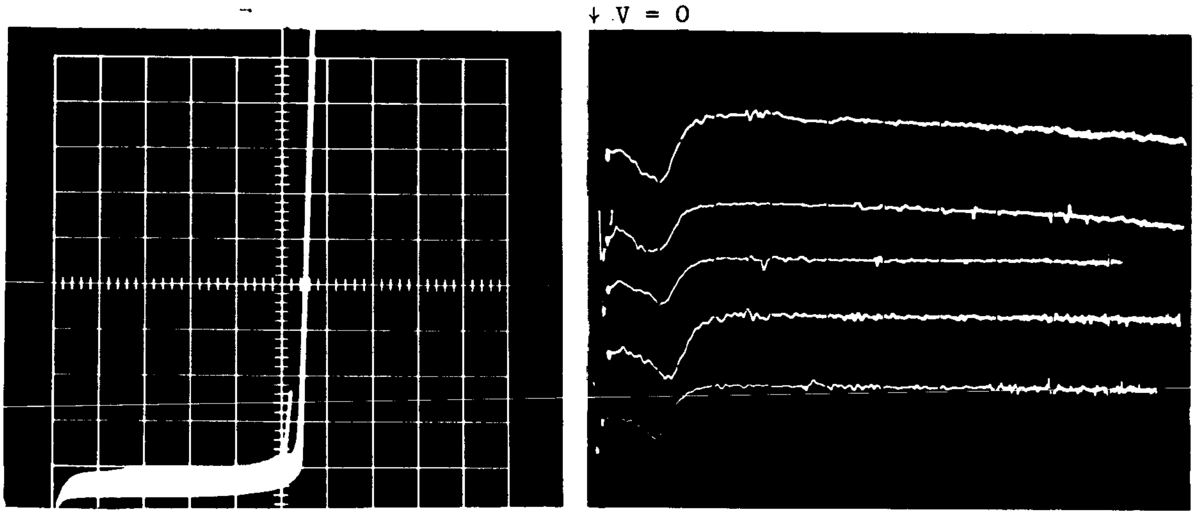

c. I-V Characteristics
Vertical 10 μ amps/major division
Horizontal 10 v/major division

d. C-V Characteristics
Vertical C/C_o
Horizontal 20 v/major division

Fig. 17. Correlation of I-V and C-V characteristics. (Each curve is a separate diode characteristic on the wafer.)

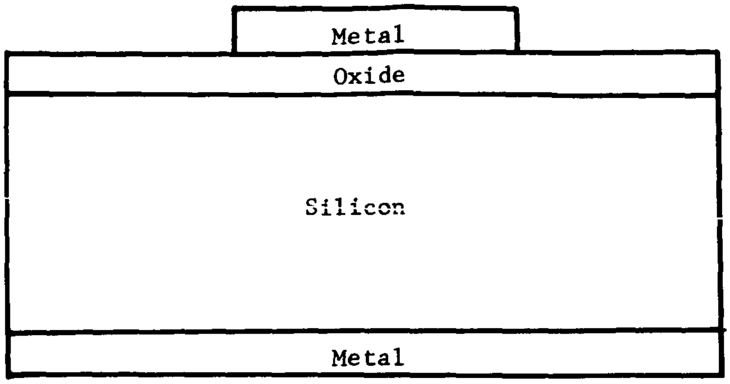

a) Conventional MOS structure

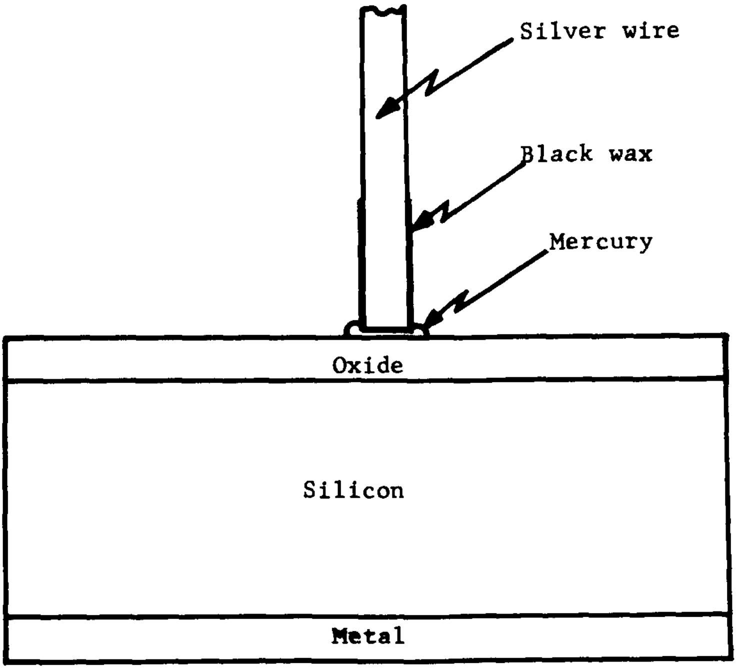

b) Mercury-tipped silver probe MOS structure

Fig. 18. Structures used to record C-V traces

To expedite the acquisition of C-V data in the fabrication process a simple liquid metal probe was used to contact the oxide surface. This probe consisted of a silver wire previously dipped into a small drop of mercury as shown in Fig. 18. The mercury wets the silver and adheres well so that the combination can be placed on the oxidized silicon surface and used to record C-V characteristics directly without evaporating a metal or otherwise contacting the oxide. Fig. 19 contrasts a trace recorded by this method with that of a nearby evaporated aluminum ring. The silver-mercury probe gives a clearer, sharper dip than the evaporated aluminum ring. Cleanliness and technique of evaporation may also influence the observed C-V characteristics but in the present experiments the clearest data came from using the silver-mercury probe. Most aluminum rings displayed extremely broad dips. The area of the silver-mercury probe is larger than that of the aluminum rings so that the total capacitance is

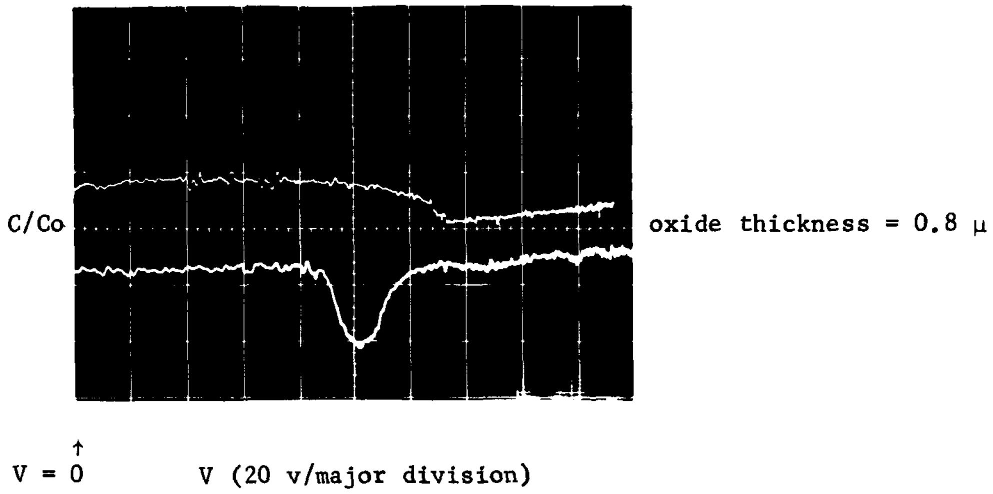

Fig. 19. Comparision of C-V trace using evaporated aluminum ring (top trace) with that of silver-mercury probe (bottom trace)

greater and the magnitude of the dip is larger. This fact does not seem to account for all the differences noted.

In addition to giving superior results the silver-mercury probe makes the data gathering simpler and perhaps less destructive. It is possible to measure the C-V characteristics at any step in the process by merely placing this probe on the oxidized surface and recording the trace. When the probe is removed, the mercury clings to the silver probe rather than the oxide, leaving a relatively clean oxide surface behind. Some surface cleaning step is advisable before proceeding with other high temperature processes, since traces of mercury will probably remain on the surface. No deleterious effects of these traces have been identified as yet, but no processing at diffusion temperatures has been attempted on such surfaces.

The significance of the surface is further emphasized by various annealing cycles which are of such low temperature-time combinations that they influence only surface properties. Several such annealing cycles are illustrated in Fig. 20 and 21. The initial I-V and C-V characteristics illustrated are those immediately following step 30 as listed in Appendix B. The aluminum has not been alloyed; but, as can be seen by comparing Figs. 20 and 21, the reverse current is high on one wafer (Fig. 20) and low on the other (Fig. 21). The corresponding V_{FB} values are high (90 - 150 v) in Fig. 20 and low ($\sim$ 20 v) in Fig. 21. An annealing cycle, consisting of heating the entire wafer at 600°C for 1 hour in 100 % oxygen, produces the characteristics shown in Fig. 20b. Similarly a 5 min annealing in hydrogen changes the characteristics of Fig. 21a into those of Fig. 21b.

The conclusions are that: (1) simple heat treatments, much too low and short to significantly affect the distribution of bulk impurities, cause drastic changes in the reverse current of planar diodes; (2) the measurement of V_{FB} is a suitable intermediate process parameter to relate to the magnitude of the reverse currents.

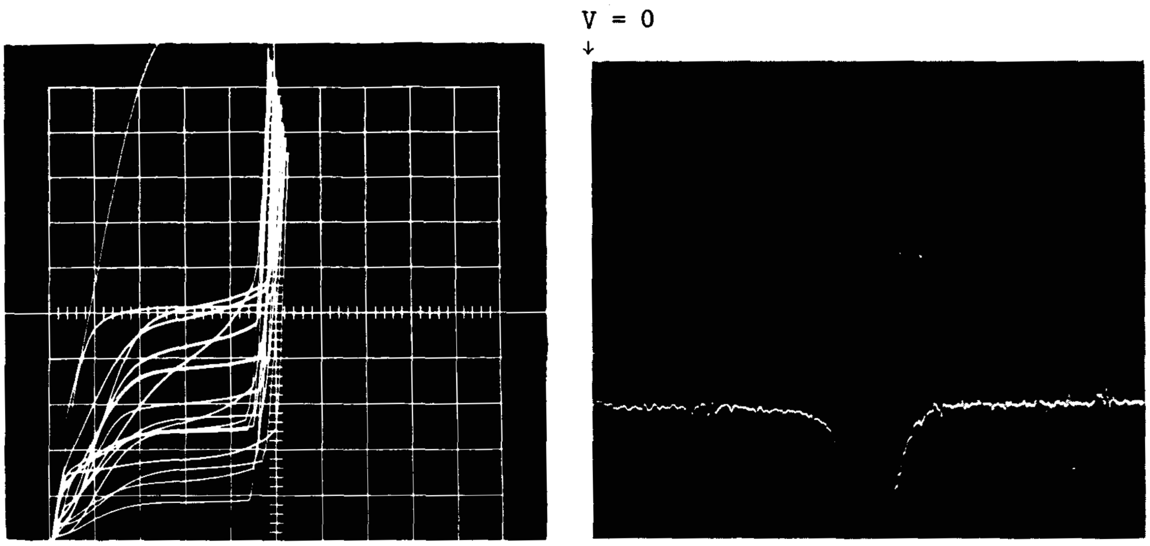

I-V Characteristics
Vertical 0.2 ma/major division
Horizontal 10 v/major division

C-V Characteristics
Vertical C/C_o
Horizontal 20 v/major division

a. Before annealing

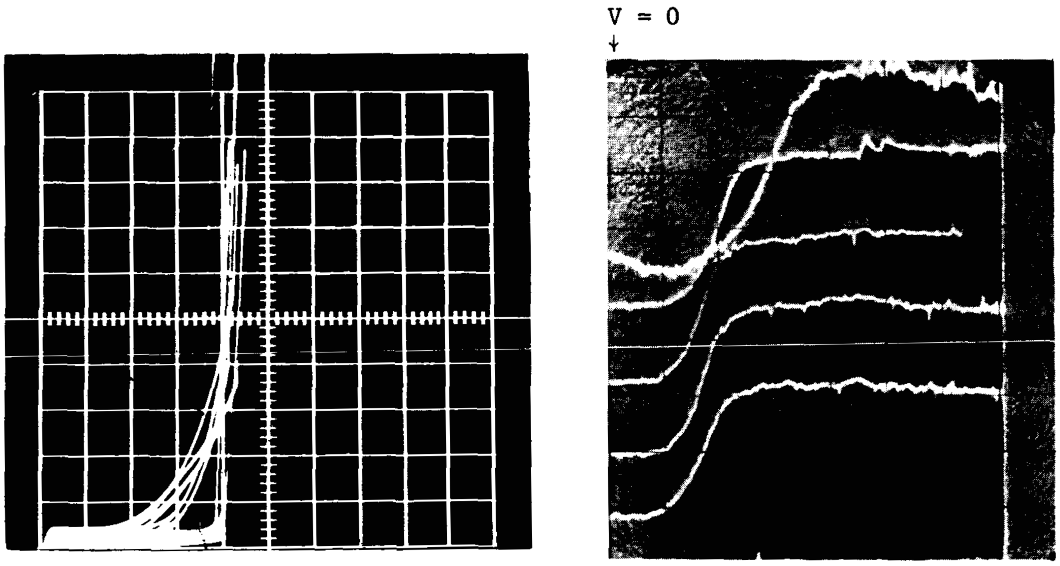

I-V Characteristics
Vertical 10 μ amp/major division
Horizontal 10 v/major division

C-V Characteristics
Vertical C/C_o
Horizontal 20 v/major division

b. After annealing cycle in oxygen

Fig. 20. The influence of annealing in oxygen (600°C, 1 hour) upon wafer electrical properties (Wafer N32). (Each curve is a separate diode characteristic on the wafer.)

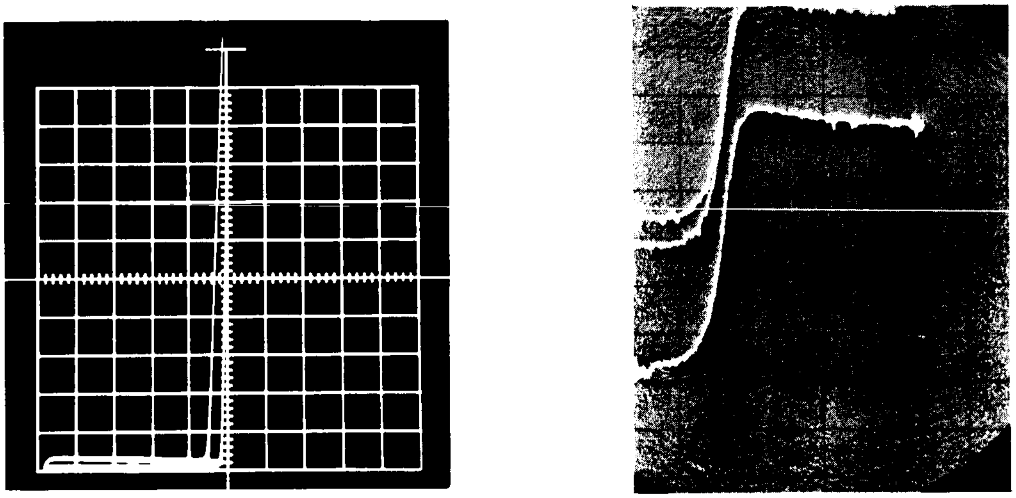

I-V Characteristics
Vertical 10 μ amp/major division
Horizontal 10 v/major division

C-V Characteristics
Vertical C/C_o
Horizontal 20 v/major division

a. Before annealing

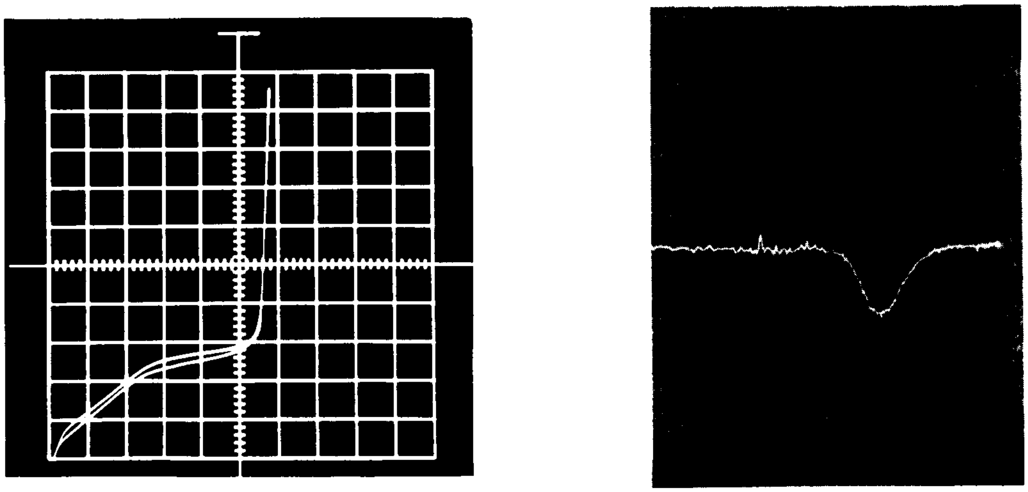

I-V Characteristics
Vertical 10 μ amp/major division
Horizontal 10 v/major division

C-V Characteristics
Vertical C/C_o
Horizontal 20 v/major division

b. After hydrogen annealing

Fig. 21. The influence of hydrogen annealing (400°C, 5 min) upon wafer electrical properties (Wafer K24). (Each curve is a separate diode characteristic on the wafer.)

6. Conclusions and Recommendations for Future Work

The models relating junction depth and sheet resistivity to the independent variables of diffusion have been revised and refined from those fitted in Ref. 1. Instead of assuming an exponential distribution of diffused impurities, the distribution assumed was that predicted by Smits (Ref. 2) plus a modification to account for the presence of impurities not measured by the four point probe. This modification is of importance only at high values of phosphorus concentration. These features form the truncated Smits model with which the data gathered in these programs were compared. The coarse fitting suggests that, for the phosphine system employed, the Smits model (with non-negligible values of K) is more realistic than the special cases usually assumed, such as the complementary error function.

While the Smits model does give a better fit to the data than previously considered models, the scatter and sequence effects noted in the data make detailed comparison less worthwhile at this time. Part of the problem has been corrected by improving the reproducibility and control over the gas flow by developing a new induction system. An analysis of variance experiment demonstrated the reduced spread in the mean values of identical runs performed at different times when using the new induction system as opposed to the old one. A repeat of some of the data points using the new system seems justified in view of the improved control now possible.

An extension of the range of independent diffusion variables has been made to include all practical values of time. Investigation of lower values of phosphine concentration should follow only after satisfactorily modeling the process in the vicinity of 35 ppm. Extending the temperature range to 1300°C and 1000°C is worthwhile right now. At the same time the 1150°C temperature could be omitted.

The errors in measuring x_j and ρ_s are not the limiting factors in fitting the data at present. The previously developed equation for x_j (Eq. 35, Ref. 1), based on the simple exponential impurity distribution, was confirmed to be valid within

20% so long as the three independent variables of diffusion remain within the following ranges:

$$1150^{\circ}C \leq T \leq 1200^{\circ}C.$$

$$30 \text{ min} \leq t \leq 60 \text{ min}.$$

$$35 \text{ ppm} \leq c \leq 2450\text{ppm}.$$

The only variable extended in this study was time. At times in excess of 100 min deeper junctions are predicted by Eq. 35, Ref. 1 than are actually observed.

The equations for predicting sheet resistivity (Eqs. 36 and 43. Ref. 1) are also restricted in time. Equation 36, valid for c = 35 or 250 ppm predicts values that are within 30% of the measured values when t = 30 minutes. For different t values, larger differences were found. Equation 43, valid for c = 2450 ppm, fits the new data best at t = 60 or 240 min. Over this range of time the values of sheet resistivity predicted by Eq. 43, Ref. 1, are within 10% of those measured at T = 1100°C or 1150°C.

All the mathematical models from Ref. 1 are based on a less realistic physical model than the truncated Smits model. At present, no explicit mathematical models relating sheet resistivity, and junction depth to t, T and c, have been developed using the truncated Smits model.

The use of the flat band voltage has been shown to be an important easily-measured intermediate process parameter which is descriptive of the surface contribution to the diode reverse current. A quantitative relationship should be derived between it and the diode reverse current. The important independent variables necessary to predict V_{FB} must be identified. The most likely independent variables for such a prediction are time and temperature of annealing cycles in specific controlled atmospheres. Other independent variables might be resistivity of the water used to generate water vapor for steam oxidation, applied electric field during oxide growth, or any quantity influencing the magnitude or distribution of impurities in the oxide.

In summary:

A. Accomplishment of the present contract:

1. An improved gas induction system, using the Hastings mass flowmeter, was developed and shown to improve reproducibility

2. The truncated Smits model has been shown to be a more realistic physical model of the diffusion process.

3. The surface parameter K for the diffusion of phosphorus into silicon has been deduced to be $10^{-2\pm2}$ μ/min at 1150°C.

4. A dependence on tube history, manifesting itself as a sequence effect at low value of diffusing impurity concentration, has been identified.

5. A silver-mercury probe has been developed as a convenient, rapid tool for measuring the C-V characteristics of oxidized silicon surfaces.

6. The flat band voltage of an oxidized silicon surface is highly correlated with the reverse current of planar p-n junctions formed under the oxide.

B. Recommendations for future work:

1. The role of the surface must be more accurately assessed. The truncated Smits model as has been described in this report assumes only one interface and neglects any surface chemical reactions. These simplifying assumptions must be justified or their effect must be otherwise accounted for in the truncated Smits model, if that model is to be truly descriptive of phosphorus diffusion into silicon in an oxidizing atmosphere.

2. The system modeled should be enlarged to include the furnace tube walls. Accounting for the impurity flow into and out of the surface of the furnace tube may lead to an understanding of the sequence effects previously described.

3. An alternative method of solution to the sequence effect problem is to develop a direct measure of the local impurity concentration surrounding the

silicon during diffusion instead of relying on a measure of the original impurity concentration.

4. The mathematical modeling of diode electrical properties should be continued using the flat band voltage of an oxidized silicon surface as an independent variable.

5. Alternatively a structure incorporating an MOS ring surrounding the diode can be used to apply a voltage (≃ the flat band voltage) which would remove the surface contribution to the diode electrical properties. The modeling development could then continue in terms of the relatively well controlled bulk diffusion process parameters employed in the manufacture of the diode structure.

6. The independent process variables that determine the magnitude of the flat band voltage must be identified.

APPENDICES

APPENDIX A

Evaluation of the Mean Ionized Impurity Concentration Using the Truncated Smits Model

1. $\bar{\eta} = \int_0^1 \eta\,du = \int_0^{u'} \left[N(u'A,B) - N(A,B)\right] du + \int_{u'}^{1} \left[N(uA,B) - N(A,B)\right] du\ , \quad (A > 0)\ ,$

as shown in Fig. A1. Note that $N(0,B) > N(A,B)$ and B must be large enough so that this is so. As B becomes small, $N(0,B)$ will become small and if B is small enough, $N(0,B) < N(A,B) = N_B$; there is then no junction and $\bar{\eta}$ is no longer defined.

2. $\frac{\bar{\eta}}{N_{eq}} = u'F(u'A,B) + \int_{u'}^{1} F(uA,B)du - F(A,B)$ by definition of the functions (Eq. 8).

3. It can be shown that (adapted from NBS AMS 55)

$$\int \mathrm{erfc}\ uA\ du = u\ \mathrm{erfc}\ uA - \frac{1}{A\sqrt{\pi}}\, e^{-(uA)^2} + \text{constant},\quad (A \neq 0).$$

$$\int e^{-(uA)^2}\mathrm{erq}(uA + B)\ du = \frac{e^{-(uA)^2}}{2AB}\ \mathrm{erq}(uA + B) - \mathrm{erq}(uA)\ + \text{constant},\quad (AB \neq 0).$$

It can also be shown that the $\lim_{B\to 0}$ of the second integral is the first.

4. If the integrals are evaluated, combined and rearranged, the answer is (letting $u'A \equiv A'$):

$$\frac{\bar{\eta}}{N_{eq}} = \frac{1}{A}\left\{ e^{-A'^2}\left[\frac{1}{\sqrt{\pi}} - A'\mathrm{erq}(A' + B) - \frac{\mathrm{erq}\ A' - \mathrm{erq}(A' + B)}{B}\right]\right.$$

$$\left. - e^{-A^2}\left[\frac{1}{\sqrt{\pi}} - A\ \mathrm{erq}(A + B) - \frac{\mathrm{erq}\ A - \mathrm{erq}(A + B)}{B}\right]\right\},\quad (A > 0)$$

5. Several special cases are of interest:

Case a. $u' = A' = 0$. (No truncation).

$$\frac{\bar{\eta}}{N_{eq}} = \frac{1}{A}\left\{\left[\frac{1}{\sqrt{\pi}} - \frac{1 - \mathrm{erq}\ B}{B}\right] - e^{-A^2}\left[\frac{1}{\sqrt{\pi}} - A\ \mathrm{erq}(A + B) - \frac{\mathrm{erq}\ A - \mathrm{erq}(A + B)}{B}\right]\right\}$$

Case b. $u' = 1,\ A' = A$ (truncation at or below N_B)

$$\frac{\bar{\eta}}{N_{eq}} = 0$$

Case c. $B \to \infty$ (the truncated erfc solution with N_o a constant)

$$\frac{\bar{\eta}}{N_{eq}} = \frac{e^{-A'^2} - e^{-A^2}}{\sqrt{\pi}\,A}$$

Case d. $B \to \infty,\ U' = A' = 0$ (the usual erfc solution)

$$\frac{\bar{\eta}}{N_{eq}} = \frac{1 - e^{-A^2}}{\sqrt{\pi}\,A}$$

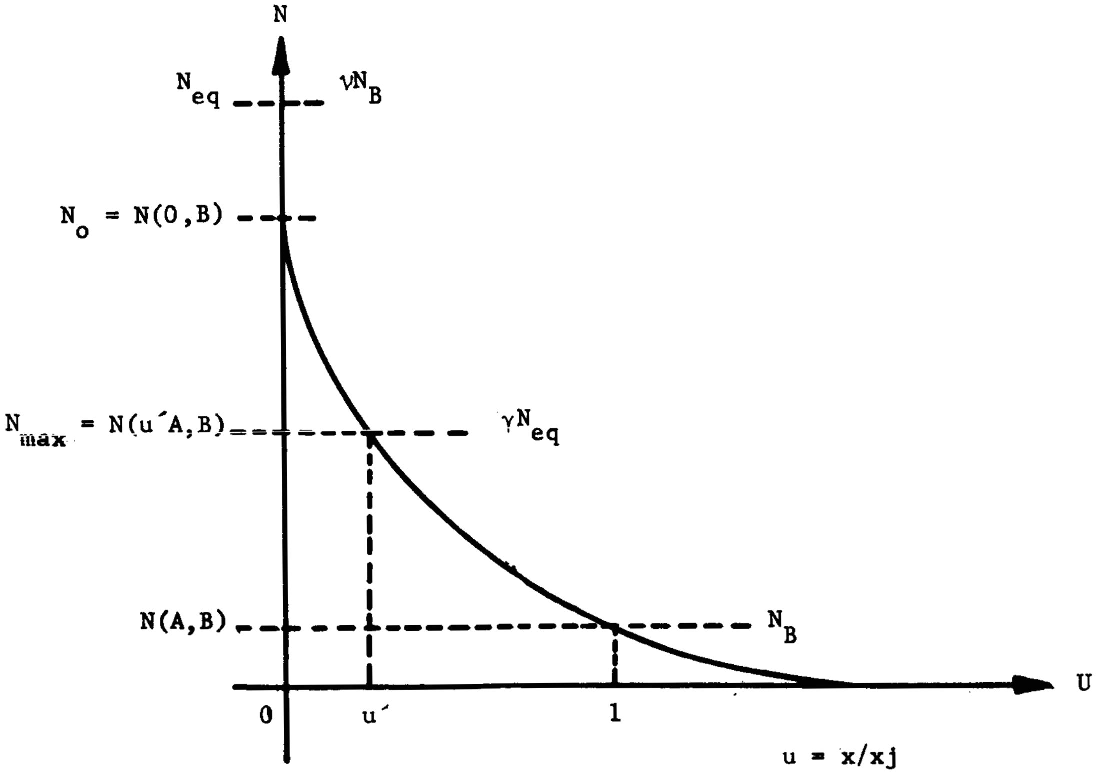

Fig. A1. Nomenclature and labels of the truncated Smits model

APPENDIX B

Procedures for Processing Wafers

1. Boil in trichloroethylene twice.
2. Rinse in methyl alcohol.
3. Flush five times with de-ionized water.
4. Heat in hot (80°C) concentrated nitric acid for twenty minutes.
5. Flush with de-ionized water five times.
6. Rinse and store in methyl alcohol.
7. Load wet onto the hot quartz boat of the oxidation furnace.
8. Oxidize in steam for 74 minutes at 1000°C.
9. Coat with 1:1 mixture of KTFR and KMER thinner immediately upon removal from the oxidation furnace.
10. Air dry overnight in a dust free enclosure or vacuum bake at ∿ 100°C for 30 minutes.
11. Print and develop mask No. 1 (Fig.B1).
12. Bake photoresist in vacuum oven at 120°C, 30 minutes.
13. Etch in buffered HF solution until etched surface becomes hydrophobic (unpatterned surface must also be etched).
14. Heat sample in hot (80°C) concentrated sulfuric acid to remove resist (20 minutes).
15. Flush in de-ionized water, 5 times.
16. Rinse and store in methyl alcohol prior to loading into the diffusion furnace.
17. Five minutes after wafer is positioned in the center of the diffusion furnace, add the desired impurity flow to the already flowing oxygen-nitrogen mixture.

a. Mask 1

b. Mask 2

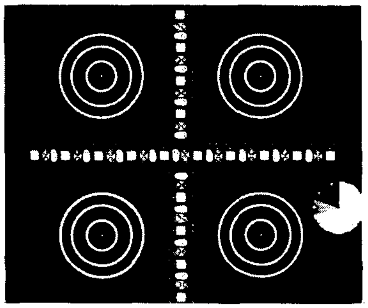

c. Mask 3

Fig. B1. Masks used in fabrication; a. Definition of diffused regions; b. Definition of ohmic contact area; c. Removal of evaporated aluminum

18. After the predetermined time has passed, turn off the impurity flow, remove the wafer rapidly (no annealing) and dip in buffered HF etch until the diffused silicon surfaces are hydrophobic.

19. Measure sheet resisitivity on both surfaces.

20. Heat in hot (80°C) concentrated nitric acid for twenty minutes.

21. Flush in de-ionized water 5 times.

22. Rinse and store in methyl alcohol prior to loading into oxidation furnace.

23. Re-oxidize wafers in steam at 1200°C, 24 minutes.

24. Repeat steps 9 to 15 using mask No. 2 (Fig. B1).

25. Dip wafer in buffered HF immediately prior to loading into the vacuum evaporator.

26. At a pressure of 5×10^{-5} torr or less and a wafer temperature of 300°C, evaporate about 1000 A of aluminum over the entire wafer.

27. Coat with photoresist immediately upon breaking the vacuum; repeating steps 9 through 12, using mask No. 3 (Fig. B1).

28. Etch aluminum in 1% aqueous sodium hydroxide solution.

29. Boil wafer in trichloroethylene and mechanically scrub off the photoresist with a cotton swab.

30. Wafer is ready for alloying or testing.

APPENDIX C

Matrix Experiment Data

a. 1100°C Data

Wafer No.	Time (min)	ρ_s ($\Omega/\square$)	x_j (Fringe)	x_j (μ)	$\rho_s x_j$ ($10^{-4}\Omega$-cm)	$\bar{\eta}$ (10^{19} cm^{-3})	$\frac{\bar{\eta}}{N_B} = J$ (10^3)	Boat Position	Run No.
c = 35 ppm									
O-21	60	36.5	4	1.07	39.1	1.8	.85	F	1
N-39	60	75.0	4	1.07	80.25	.7	.350	B	
T-9	15	90.5	2	.54	49.0	1.35	0.58	F	2
O-20	15	200.0	2	.54	108	.44	.209	B	
O-16	240	7.20	11	2.94	21.2	3.6	1.71	F	3
N-32	240	13.0	9	2.41	31.4	2.1	1.05	B	
N-31	30	41.0	3	.80	32.8	2.2	1.10	F	4
O-17	30	90.0	3	.80	72.0	.8	.38	B	
N-25	960	2.00	26	6.96	13.9	5.6	2.80	F	5
O-22	960	3.95	21	5.62	22.2	3.8	1.80	B	
c = 250 ppm									
L-33	240	1.35	19	5.08	6.85	14	7.3	B	20
N-50	240	1.20	19	5.08	6.10	17	8.5	F	
P-12	30	4.00	8	2.14	8.56	10	4.5	F	21
O-8	30	3.70	9	2.41	8.91	9.4	4.47	B	
T-6	60	2.50	10	2.68	6.70	14	6.0	B	22
P-10	60	2.05	11	2.94	6.03	17	8.7	F	
T-8	15	6.60	6	1.60	10.55	8.0	3.47	F	23
P-14	15	6.75	6	1.60	10.8	7.9	3.59	B	
K-21	960	0.70	34	9.10	6.37	16	8.8	F	24
P-11	960	0.67	35	9.36	6.27	17	7.7	B	
c = 2450 ppm									
J-19	240	0.60	24	6.42	3.85	41	24.1	F	25
K-30	240	0.54	25	6.69	3.61	43	23.8	B	
P-24	30	1.95	9	2.41	4.69	28	12.7	F	26
J-20	30	1.85	10	2.68	4.95	23	13.5	B	
J-23	60	1.45	13	3.48	5.04	23	13.5	F	27
K-26	60	1.20	14	3.75	4.50	27	15	B	
O-25	15	2.85	8	2.14	6.09	17	8.0	F	28
J-18	15	2.6	7	1.87	4.86	28	16.4	B	

NOTES:

1. Column headed ρ_s lists the sixth highest of the eight values of sheet resistivity measured on the unpatterned side of the wafer.
2. Column headed x_j (fringe) represents a median of either 5 or 9 measured fringe values.
3. Column headed x_j (μ) is the number of fringes multiplied by 0.2675 ($\lambda/2$ for the green line of thallium).

APPENDIX C

Matrix Experiment Data

b. 1150°C Data

Wafer No.	Time (min)	ρ_s (Ω/□)	x_j (Fringe)	x_j (μ)	$\rho_s x_j$ (10^{-4} Ω-cm)	$\bar{n}$ (10^{19} cm^{-3})	$\frac{\bar{n}}{N_B} = J$ (10^3)	Boat Position	Run No.
				c = 35 ppm					
O-23	60	54.5	6	1.61	87.7	.62	.295	F	6
O-15	60	75	5	1.34	101	.49	.233	B	
O-18	15	200	2	.535	110	.43	.204	F	7
N-34	15	185	3	.803	148	.25	.125	B	
T-24	240	8.25	15	4.01	33.1	2.15	.93	F	8
N-26	240	7.40	15	4.01	30.1	2.8	1.40	B	
L-74	30	26.5	5	1.34	35.5	2.0	1.05	F	9
K-70	30	36.0	5	1.34	48.2	1.32	.73	B	
P-25	960	4.4	30	8.03	35.3	2.0	.90	F	10
K-57	960	4.45	29	7.76	34.5	2.05	1.13	B	
				c = 250 ppm					
K-62	240	1.10	25	6.69	7.35	12.5	6.9	F	11
L-73	240	1.10	25	6.69	7.35	12.5	6.5	B	
L-76	30	4.10	10	2.68	11.0	7.3	3.84	F	12
K-59	30	4.00	9	2.41	9.64	8.5	4.72	B	
K-28	60	2.45	13	3.48	8.52	10	5.5	F	13
L-34	60	2.50	13	3.48	8.70	9.9	5.21	B	
L-31	15	5.90	7	1.87	11.0	7.3	3.84	F	14
K-61	15	6.40	7	1.87	12.0	6.6	3.66	B	
L-25	960	.58	48	12.8	7.42	12.3	6.4	F	15
K-23	960	.51	52	13.9	7.08	13	7.2	B	
				c = 2450 ppm					
K-17	240	.46	34	9.10	4.18	32	17.7	F	16
N-38	240	.44	34	9.10	4.00	36.5	18.2	B	
K-63	30	1.40	14	3.75	5.25	21	11.6	F	17
K-24	30	1.45	13	3.48	5.04	23	12.7	B	
N-23	60	1.10	16	4.28	4.70	26.5	13.2	F	18
K-27	60	1.00	17	4.55	4.55	30	16.6	B	
N-29	15	2.10	10	2.68	5.62	19	9.5	F	19
K-15	15	2.00	10	2.68	5.36	21	11.6	B	

NOTES:

1. Column headed ρ_s lists the sixth highest of the eight values of sheet resistivity measured on the unpatterned side of the wafer.
2. Column headed x_j (fringe) represents a median of either 5 or 9 measured fringe values.
3. Column headed x_j (μ) is the number of fringes multiplied by 0.2675 (λ/2 for the green line of thallium).

APPENDIX C

Matrix Experiment Data

c. 1200°C Data

Wafer No.	Time (min)	ρ_s ($\Omega/\square$)	x_j (Fringe)	x_j (μ)	$\rho_s x_j$ ($10^{-4}\Omega$-cm)	$\bar{\eta}$ (10^{19} cm^{-3})	$\frac{\bar{\eta}}{N_B} = J$ (10^3)	Boat Position	Run No.
c = 35 ppm									
T-7	240	8.0	20	5.35	42.8	1.58	.686	F	29
K-29	240	12.5	20	5.35	66.9	.90	.50	B	
T-22	30	53.0	7	1.87	99.1	.50	.217	F	30
P-22	30	57.0	7	1.87	107	.46	.209	B	
L-70	60	23.5	10	2.68	63.0	.95	.50	F	31
P-20	60	33.0	10	2.68	88.4	.60	.273	B	
T-20	15	89	4	1.07	95.2	.53	.23	F	32
P-21	15	125	4	1.07	134	.30	.136	B	
L-71	960	6.8	41	10.97	74.6	.75	.395	F	33
T-21	960	6.3	42	11.24	70.8	.80	.348	B	
c = 250 ppm									
T-19	240	1.35	31	8.29	11.2	7.0	3.04	F	34
L-30	240	1.25	32	8.56	10.7	7.8	4.11	B	
L-27	30	3.85	12	3.21	12.4	6.2	3.26	F	35
T-13	30	3.90	11	2.94	11.5	6.8	2.96	B	
T-18	60	2.15	17	4.55	9.78	8.5	3.70	F	36
N-26X	60	2.25	17	4.55	10.2	8.0	4.0	B	
T-17	15	6.20	8	2.14	13.3	5.9	2.57	F	37
O-11	15	5.55	8	2.14	11.9	6.7	3.19	B	
P-19	960	.68	66	17.66	12.0	6.6	3.0	F	38
L-32	960	.61	70	18.73	11.4	7.0	3.68	B	
c = 2450 ppm									
N-28	240	.39	45	12.04	4.69	27	13.5	F	39
P-17	240	.38	45	12.04	4.57	28	12.7	B	
T-14	30	1.20	17	4.55	5.46	20	8.69	F	40
O-13	30	1.20	17	4.55	5.46	20	9.52	B	
T-16	60	.61	25	6.69	4.08	34	14.8	F	41
P-23	60	.52	28	7.49	3.89	39	17.7	B	
K-19	15	1.55	13	3.48	5.39	21	11.6	F	42
T-13X	15	1.55	12	3.21	4.97	26	11.3	B	

NOTES:

1. Column headed ρ_s lists the sixth highest of the eight values of sheet resistivity measured on the unpatterned side of the wafer.
2. Column headed x_j (fringe) represents a median of either 5 or 9 measured fringe values.
3. Column headed x_j (μ) is the number of fringes multiplied by 0.2675 ($\lambda/2$ for the green line of thallium).

References

1. Research Triangle Institute, Diffusion Process Modeling, by Robert P. Donovan, Technical Summary Report, Contract No. NAS8-11243, Durham, North Carolina, May 1964 - December 1964 (U).
2. F. M. Smits, "Formation of Junction Structures by Solid State Diffusion," Proc. IRE 46, June 1958, pp. 1049-1061.
3. Research Triangle Institute, Solid State Laboratory Technical Note No. 16, "Definition, Applications, and Properties of the ERQ, a New Function," by R. A. Evans.
4. E. Kooi, "Formation and Composition of Surface Layers and Solubility Limits of Phosphorus During Diffusion in Silicon," J. Electrochem. Soc. 111, December 1964, pp. 1383-1387.
5. E. Tannenbaum, "Detailed Analysis of Thin Phosphorus-Diffused Layers in p-type Silicon," Solid State Electronics 2, March 1961, pp. 123-132.
6. H. G. Carlson, S. S. Baird, and C. A. Kossack, "Some Aspects of Phosphorus Diffusion in Silicon," Extended Abstracts of Electronics Division 14, The Electrochemical Society Inc., May 1965, pp. 287-289 (abstract of paper presented at the Spring Mtg., May 1965, San Francisco, California).
7. E. A. Corl, "Anion Reaction for Failure Analysis of Microcircuit Components," Physics of Failure in Electronics, Volume 3, edited by M. F. Goldberg and J. Vaccaro, RADC series in Reliability, 1965, pp. 342-353.
8. Research Triangle Institute, Integrated Silicon Device Technology Volume VI, Unipolar Transistors, by J. R. Hauser, Technical Report No. ASD-TDR-63-316, Vol VI, Contract No. AF 33(615)-1998, Durham, N. C., March 1965 (U) AD-613 915.
9. Research Triangle Institute, Integrated Silicon Device Technology Volume IV----Diffusion, by A. M. Smith, Technical Documentary Report No. ASD-TDR-63-316, Vol. IV, Contract AF 33(657)-10340, Durham, North Carolina, February 1964 (U) AD-603-716.
10. W. R. Runyan, Silicon Semiconductor Technology, McGraw-Hill Book Co., 1965, pp. 123-124.